https://doi.org/10.5194/wes-2026-9
Preprint. Discussion started: 10 February 2026

WIND ENERGY SCIENCE DISCUSSIONS
Open Access

Edgewise instabilities of a wind turbine blade section in attached flow conditions

Hendrik Verdonck[1] and Oliver Hach[1]

[1]German Aerospace Center (DLR), Institute of Aeroelasticity, Göttingen, Germany

Correspondence: Hendrik Verdonck (hendrik.verdonck@dlr.de)

Abstract.

With the persistent trend towards larger, lighter turbine blades and the resulting increase in blade flexibility, the risk of edgewise instabilities is elevated. This emphasizes the need for a better understanding of the accuracy of simulation models and the mechanisms affecting the damping of edgewise modes. This study investigates edgewise instabilities in wind turbines under attached flow conditions using a two-dimensional, three-degree-of-freedom typical section model. The primary goal of this work is to validate the stability analysis predictions from common low-fidelity aerodynamic models by comparing them with a high-fidelity computational fluid dynamics (CFD) reference result. In addition, the study aims to deepen the understanding of the fundamental mechanisms behind edgewise instabilities. The comparison of the stability analysis results obtained with aerodynamic models of different fidelity demonstrates excellent agreement in both the trends and quantitative damping predictions for the edgewise mode. An additional sensitivity study highlights the importance of the steady load vector on the damping prediction. The flutter mechanism analysis shows that the edgewise instabilities are caused by a coupling of flapwise motion with the structurally coupled edgewise-torsional motion. Edgewise instabilities can occur when there is sufficient structural edge-twist coupling, both in edge-twist coupling to stall or edge-twist coupling to feather. The findings in the paper increase the confidence in common low-fidelity aerodynamic models and contribute to a better understanding of edgewise instabilities.

1 Introduction

To reduce overall costs and enhance the efficiency of wind turbines, there has been a persistent trend towards larger rotor sizes, while simultaneously striving to minimize rotor blade weight. These new designs, and potentially even larger and lighter designs in the future, lead to increased blade flexibility, resulting in new aeroelastic characteristics for both the rotor blades and the turbine as a whole. This, however, introduces the potential for unfavorable or unforeseen aeroelastic phenomena. To mitigate these risks, it is essential to deepen our understanding of these phenomena, particularly those that are more likely to occur in future designs. Additionally, it is necessary to assess whether current industry-standard design tools and aeroelastic models can accurately capture the relevant physics.

One specific aeroelastic issue that has recently regained attention is edgewise instabilities. Previously, this topic was the focus of significant research, particularly in relation to stall-induced edgewise vibrations in stall-controlled wind turbines

https://doi.org/10.5194/wes-2026-9
Preprint. Discussion started: 10 February 2026

eawe european academy of wind energy
Open Access WIND ENERGY SCIENCE DISCUSSIONS

(Hansen, 2007; Chaviaropoulos, 2001). At that time, such turbines were more common, but stall-controlled designs are now largely outdated, and the turbine designs investigated in the early 2000s no longer reflect current design trends. Today, edgewise instabilities are attracting renewed interest due to their relevance under a range of different operating conditions.

Edgewise instabilities are occurring as vortex-induced and stall-induced vibrations, especially during standstill or idling conditions where wind inflow directions could be uncontrolled. These instabilities pose a real challenge for current turbine designs (Pirrung et al., 2024; Bangga, 2025). However, this work will not focus on this kind of instabilities caused by flow separation under off-design conditions. Instead, the focus will be on the damping and instabilities of edgewise modes under nominal, attached flow conditions. Therefore, from this point forward, all references to edgewise instabilities will pertain exclusively to those occurring in attached flow conditions.

The relevance of this topic is supported by several studies. For instance, Kallesøe and Kragh (2016) and Volk et al. (2020) reported that an edgewise flutter-like instability was observed during overspeed operation in experimental tests on a 7 MW Siemens-Gamesa turbine. Additionally, Peng (2025) presented experimental blade root load data from 6+MW Goldwind prototype turbines. These turbines were tested with both an initial blade design and a lighter, reduced-torsional-stiffness blade design, operated under a special controller that allowed for higher rotational speeds. The data showed significantly increased standard deviations in the blade root edgewise moment for the lighter blade design at higher speeds. The wind speeds at which these increased loads were observed matched well with the wind speeds where the linearized model predicted negative damping. Furthermore, Verdonck et al. (2024) found that the stability margin of the IEA 15 MW reference wind turbine was small, and minor changes in the center of gravity and shear center positions along the chord resulted in an aeroelastically unstable blade design.

Multiple studies investigated edgewise instabilities and its sensitivities on full turbine models. Griffith and Chetan (2018) and Chetan et al. (2021) compared the flutter characteristics between multiple, large two-bladed downwind and three-bladed rotors. They concluded that the critical inflow speed for edgewise flutter mechanisms tends to be lower than the critical classical flutter speed for three-bladed rotors, while two-bladed rotors show an opposite trend with in most cases a more critical classical flap-twist flutter mechanism. Wanke et al. (2020) presented a sensitivity study on the damping of the 1st edgewise modes comparing upwind and downwind configurations and noticed an increase in damping for the upwind configuration. Kelley and Paquette (2020) showed a numerical flutter investigation for large wind turbine blades designed with increased flexibility to be transportable by train. Their investigation showed an edgewise instability mechanism below rated speed attributable to the increased flexibility of the blade design. They furthermore showed that the aerodynamic lift and moment caused by harmonic edgewise motion did not significantly change the flutter speed. Xia et al. (2026) performed a sensitivity study on the influence of local structural variations on the classical flutter and edgewise flutter limit for the DTU 10 MW turbine, observing the highest sensitivity for the torsional stiffness in the mid part of the rotor blade. Zhou et al. (2018) investigated the influence of structural flap-twist coupling introduced by unbalanced skin laminates on classical flutter and edgewise instabilities. They observed no significant influence of the flap-twist coupling on the flutter speed. Note that the maximum parametric coupling introduced, –0.05 at the blade tip, is relatively small compared with the projected flap-twist coupling values of up to –0.4 foreseen for future aeroelastically tailored wind turbine blades (Bottasso et al., 2013).

https://doi.org/10.5194/wes-2026-9
Preprint. Discussion started: 10 February 2026

When it comes to unravel and explain the fundamental mechanisms of specific instabilities, the most established approach is to reduce the complexity down from a full turbine with a large number of degrees of freedom to a typical airfoil section with two or three degrees of freedom (Bisplinghoff and Ashley, 1962). This approach has been used numerous times to successfully improve the understanding of aeroelastic phenomena on wind turbine blades. Hansen (2007) used a typical section to explain the influence of the vibration direction on the damping and to demonstrate a classical flutter mechanism. Rasmussen et al. (1999) and Chaviaropoulos et al. (2003) used a typical section to analyze blade vibrations in stalled conditions respectively with low-fidelity and high-fidelity aerodynamic models. As a promising new approach, Branlard et al. (2024) introduced a generalized cross section as a reduced order model, deriving its structural dynamics from the full blade's generalized degrees of freedom, thereby establishing a closer link between the dynamics of the reduced order model and the full blade.

A thorough and insightful explanation of the fundamental mechanism principles for edgewise instabilities has been given for a three-degree-of-freedom blade section by Stäblein et al. (2017a). In this study the focus was on the influence of structural edge-twist and flap-twist coupling on the stability of the blade section, indicating in detail the importance of especially the edge-twist structural coupling towards the damping of edgewise modes and towards the edgewise instability mechanisms. These findings are supported by the work of Kallesøe (2011), which showed that the edgewise damping of a full blade model computed with a linearized model depends strongly on the non-linear equilibrium point about which is linearized, and by Stäblein et al. (2017b) in a further full blade and full turbine analysis for the DTU 10 MW turbine, showing again a strong sensitivity of the damping of the first edgewise mode on the structural edge-twist coupling, but additionally showing that this sensitivity depends strongly on the operating point.

Altogether, this literature provides a good understanding of the edgewise instability phenomenon. It is a flutter problem with many similarities to the classical flap-twist flutter mechanism. Much like classical flap-twist flutter, the phase angle between flapwise and torsional motion plays a key role. If the torsional motion leads flapwise motion, the flapwise force induced by torsional motion will perform positive work, which can lead to an instability if not sufficiently counteracted by the dampening flapwise force induced by flapwise motion. The main difference is the origin of the torsional motion. In classical flutter, the torsional motion originates from a direct structural and aerodynamic coupling between flapwise and torsional motion, in edgewise flutter, the torsional motion is introduced by the structural edge-twist coupling. Therefore, in order for edgewise instabilities to form, there has to be sufficient structural edge-twist coupling. Another aspect in which it seems to differ from classical flap-twist flutter is the gradient of the damping with respect to the relative wind speed at the critical flutter speed. In a classical mechanism the coupled flap-torsional mode is normally highly damped, but small differences in the flap-torsional phase can lead to a strong reduction in the damping. This also implies that just a small increase of the relative wind speed could change the damping from strongly positive to critically negative. As far as published so far, edgewise instabilities are characterized by a much more forgiving soft flutter tendency (Chetan et al., 2021; Kelley and Paquette, 2020; Volk et al., 2020). Edgewise modes are always lowly damped, and the observed gradients of the damping with respect to the relative wind speed are small, also at the point of instability.

The aeroelastic models used for the design and certification of wind turbines typically consist of non-linear beam models to represent the most important structural dynamic components and a low-fidelity aerodynamic model based on blade element

https://doi.org/10.5194/wes-2026-9
Preprint. Discussion started: 10 February 2026

eawe european academy of wind energy
Open Access WIND ENERGY SCIENCE DISCUSSIONS

momentum (BEM) theory with empirical or potential theory based extensions for unsteady airfoil aerodynamics and unsteady wake effects (Collier et al., 2024). Similarly, most investigations on edgewise instabilities in nominal operating conditions have been done with models of this level of fidelity. An exception are the recent studies by Hermes (2024); Hermes et al. (2025), who compared the stability analysis based on CFD aerodynamics with different low-fidelity BEM methodologies for the IEA 10 MW turbine in operational conditions. The observed differences in the damping for the edgewise modes were relatively small in operating conditions with axially aligned inflow, larger differences up to 30% were shown for yaw misaligned conditions. The analysis was only done for stable configurations and operating points. The typical subsonic, high Reynolds number, moderate angle of attack flow in nominal operating conditions justifies the assumptions that underlie low-fidelity potential theory based models. Nevertheless, the question remains whether the low-fidelity aerodynamic model assumptions lead to any noticeable quantitative error in the damping prediction, especially for modes or flutter mechanisms including a lot of edgewise movement, also considering the relatively thick profiles of wind turbine blades, which is not immediately accounted for in low-fidelity models.

This work builds upon the study by Stäblein et al. (2017a) on the two-dimensional, three-degree-of-freedom typical section. Wherever possible the same model, conventions and cases will be used. In contrast to the work by Stäblein et al., the focus will be more on the damping of the edgewise mode and less on the general influence of structural bend-twist coupling on the overall aeroelastic properties. This presented work serves a couple goals. The first goal is to asses the influence of aerodynamic modeling. A high-fidelity CFD result will be introduced which will serve as reference for a low-fidelity model and the literature result. The goal is to show whether there is a noticeable quantitative difference in the damping of the edgewise mode between the high-fidelity and low-fidelity results, as well as to identify which terms in the aerodynamic modeling have the highest sensitivity. As such, this study can be seen as a validation exercise of common low-fidelity aerodynamic modeling for the damping prediction of edgewise modes. The second main goal is to elaborate further on the fundamental mechanism of the instability. Finally, in the process of this work some mistakes were discovered in the original publication by Stäblein et al. (2017a). This work therefore intents to serve as corrigendum for the original paper.

First, in section 2 the investigated model, basic methodology and the different aerodynamic models will be introduced. This also includes a discussion of the required corrections for the methodology presented in Stäblein et al. (2017a). Secondly, in section 3 the stability analysis results for the different aerodynamic models are compared for cases with varying structural coupling and steady load. Then, in section 4 sensitivities of specific components in the low-fidelity aerodynamic models are further detailed. And finally, in section 5 the fundamental instability mechanism are explored.

2 Methodology

This section introduces first the investigated aeroelastic system and its equation of motion, followed by a discussion of the different analysis methods and aerodynamic methodologies.

A three-way comparison will be made in this study. The first two methodologies strictly differ in the aerodynamic model, where one uses a high-fidelity CFD model and the second a low-fidelity potential theory based model. Both methodologies

https://doi.org/10.5194/wes-2026-9
Preprint. Discussion started: 10 February 2026

Open Access WIND ENERGY SCIENCE DISCUSSIONS

use a frequency domain flutter analysis approach to obtain the modal properties as a function of the relative wind speed. The frequency domain flutter analysis approach is explained in section 2.2, and the methodology to obtain the high-fidelity and low-fidelity frequency domain aerodynamic forces in section 2.2.1 and 2.2.2. The third methodology in the comparison is the literature reference presented in Stäblein et al. (2017a). This approach relies on a similar low-fidelity potential theory based aerodynamic model, but uses a direct linearization of the equations of motion to derive a state-space model which allows to obtain the modal properties of the system by an eigenvalue analysis of the state-transition matrix.

2.1 Model and equations of motion

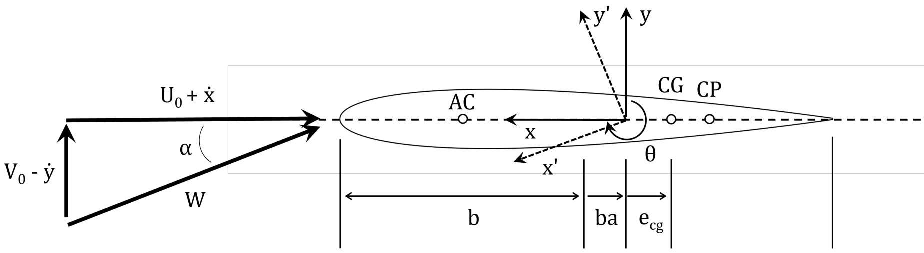

Figure 1. Model Overview. Note that for the investigated model a = -0.431 and $e_{cg} = 0.304m$, which implies that the elastic axis is slightly aft of the AC, followed by the center of gravity at a relatively close distance.

This study investigates the same two-dimensional, three-degree-of-freedom typical section as proposed by Stäblein et al.. An overview of the model and its dimensions is given in figure 1. The half-chord length is defined as b, the position of the elastic axis is defined relative to the half-chord point as a fraction of b with the non-dimensional parameter a, and the center of gravity position e_{cg} is defined relative to the elastic axis. The steady wind speed along the chord is U_0, the steady wind speed perpendicular to the chord is V_0 and the total velocity vector, including the relative velocity of the section is W. The three coordinates x, y and θ represent respectively edgewise motion parallel to the chord, flapwise motion perpendicular to the chord and torsional rotation around the elastic axis. Note that this deviates from the more common convention for typical sections where the degrees of freedom are defined perpendicular and parallel relative to the inflow, indicated in the figure by x' and y', rather than relative to the chord. The structural degrees of freedom are gathered in the vector $\mathbf{q} = \{x, y, \theta\}^T$ and the equations of motion for this system in matrix form are given as

$$\mathbf{M}_{\text{s}}\ddot{\mathbf{q}} + \mathbf{C}_{\text{s}}\dot{\mathbf{q}} + \mathbf{K}_{\text{s}}\mathbf{q} = \mathbf{f}_{\text{A}}(t, \ddot{\mathbf{q}}, \dot{\mathbf{q}}, \mathbf{q}, \alpha_0), \text{ with} \tag{1}$$

$$\mathbf{M}_{\text{s}} = \begin{bmatrix} m & 0 & 0 \\ 0 & m & -me_{cg} \\ 0 & -me_{cg} & m\left(e_{cg}^2 + r^2\right) \end{bmatrix}, \quad \mathbf{C}_{\text{s}} = \mathbf{\Phi}^{-T} \begin{bmatrix} 2\zeta_{\tilde{x}}\omega_{\tilde{x}} & 0 & 0 \\ 0 & 2\zeta_{\tilde{y}}\omega_{\tilde{y}} & 0 \\ 0 & 0 & 2\zeta_{\tilde{\theta}}\omega_{\tilde{\theta}} \end{bmatrix} \mathbf{\Phi}^{-1}, \quad \mathbf{K}_{\text{s}} = \begin{bmatrix} k_x & 0 & k_{x\theta} \\ 0 & k_y & k_{y\theta} \\ k_{x\theta} & k_{y\theta} & k_\theta \end{bmatrix}. \tag{2}$$

The aerodynamic force vector $\mathbf{f}_{\text{A}}$ in theory depends on many other parameters, amongst others the Reynolds number and Mach number. However, these effects are small for this application and are therefore fixed, such that the aerodynamic forces

https://doi.org/10.5194/wes-2026-9
Preprint. Discussion started: 10 February 2026

only depend on time t, the structural motion of the section $\ddot{\mathbf{q}}, \dot{\mathbf{q}}, \mathbf{q}$, and the steady angle of attack α_0. The properties of the mass matrix $\mathbf{M}_\mathrm{s}$ are the mass m of the blade section, the position of the center of gravity relative to the elastic axis e_{cg}, and the radius of gyration with respect to the center of gravity r. The properties of the stiffness matrix $\mathbf{K}_\mathrm{s}$ are defined as

$$k_x = m\omega_x^2, \quad k_y = m\omega_y^2, \quad k_\theta = J\omega_\theta^2, \quad k_{x\theta} = -\gamma_x\sqrt{k_x k_\theta}, \quad k_{y\theta} = -\gamma_y\sqrt{k_y k_\theta} \tag{3}$$

with the uncoupled edgewise, flapwise and torsional eigenfrequencies, ω_x, ω_y, ω_θ, the rotational inertia around the elastic axis $J = m\left(e_{cg}^2 + r^2\right)$, and the edge-twist and flap-twist coupling parameters γ_x and γ_y. The definition of these coupling parameters was introduced by Lobitz and Veers (1998). A positive edge-twist coupling parameter γ_x implies a twist to stall coupling for an edgewise movement towards the leading edge, a negative γ_x coupling implies twist to feather. A positive flap-twist coupling parameter γ_x implies pitch to stall for flapwise motion towards the suction side, a negative flap-twist coupling parameter implies pitch to feather. For realistic, full turbine systems, the edge-twist coupling is mainly driven by the out-of-plane deflection of the blade, either by prebend or by flapwise deformation under load. A prebend deflection upwind typically implies a positive edge-twist coupling in this convention, flapwise deformation downwind typically implies a negative edge-twist coupling. The flap-twist coupling is mainly driven by the structural layout of the blade, whereby especially negative pitch-to-feather couplings could be favorable with respect to load reduction (Bottasso et al., 2013). The structural damping is introduced in the form of a proportional damping matrix $\mathbf{C}_\mathrm{s}$, with the modal matrix from the mass normalized mode shapes Φ, and the critical damping ratios and natural frequencies of the coupled blade section, respectively $\zeta_{\tilde{q}}$ and $\omega_{\tilde{q}}$. For further details on the aeroelastic model, please refer to Stäblein et al. (2017a).

Model parameters

The model parameters used in this study are for the most part identical to those defined in Stäblein et al. (2017a), and are listed in Table 1. These values are representative for a blade section at 75% blade radius for the DTU 10 MW reference wind turbine. The uncoupled eigenfrequencies and damping ratios are those for the first edgewise, flapwise and torsional mode of the full blade. Figure 2 shows the model once more with all parameters located as defined for this study.

Table 1. Geometrical and structural blade section parameters

ω_x	0.93 Hz	ω_y	0.61 Hz	ω_θ	6.66 Hz	$\zeta_{\tilde{x}}$	0.0049	$\zeta_{\tilde{y}}$	0.0047	$\zeta_{\tilde{\theta}}$	0.0093
c	3.292 m	m	203 $\mathrm{kg\,m^{-1}}$	r	0.785 m	e_{cg}	0.304 m	a	−0.431		

Two operating angles of attack will be investigated in this work. The first angle of attack of 7° is representative for a design angle of attack in the outboard section of a wind turbine rotor blade, e.g. for the DTU wind turbine it is approximately the angle of attack at 75% blade radius for a wind speed of $8\,\mathrm{m\,s^{-1}}$ and induction factor of 0.3. Secondly, stability analysis results with a much lower angle of attack of 0° will be shown, to investigate the effect of the steady load. Note that due to the zero-lift angle of attack, the steady lift is not zero at 0° angle of attack.

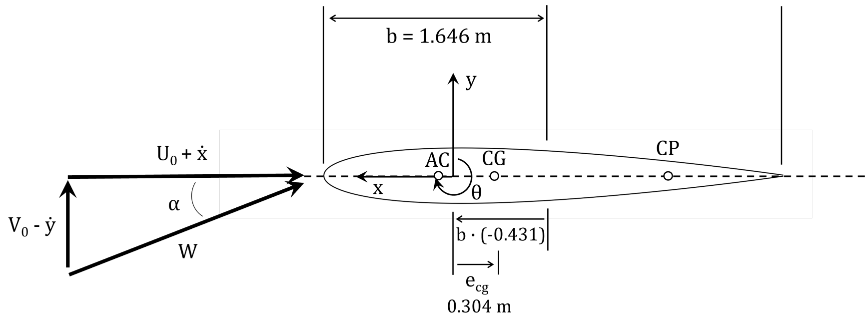

Figure 2. Model overview with parameters defined for this study.

The FF-W3-241 aerodynamic profile, which corresponds to the airfoil shape at 75% blade radius of the DTU 10 MW turbine, is used for the CFD analysis. Although the blade thickness at this location is slightly lower than the 24.1% of this profile, no adjustment was made to the profile thickness in this study. The steady CFD results were used to adjust some model parameters
180 used in both low-fidelity models. The zero-lift angle of attack, $\alpha_{L=0}$, is $-3°$. The gradient of the lift polar, the moment coefficient around the aerodynamic center due to the profile camber, and the drag coefficient were tuned as summarized in Table 2. As the model is not perfectly linear, different values were used for the analysis at $0°$ and $7°$ angle of attack.

Table 2. Steady airfoil properties

AOA	C_{L_α}	$C_{M_{AC}}$	C_{D_0}
0°	7.23	-0.27	0.010
7°	6.62	-0.31	0.014

2.2 Frequency domain flutter analysis

To assess the stability of the coupled blade section a frequency domain flutter analysis is performed. The equation of motion
185 in Eq. 1 is transformed into the Laplace domain by assuming a damped harmonic solution of the form

$$\mathbf{q} = \widehat{\mathbf{q}} e^{\frac{W_0}{b} pt}, \tag{4}$$

with the amplitude $\widehat{\mathbf{q}}$ and the non-dimensionalized Laplace variable $p = g + \mathrm{i}k$, where the non-dimensional damping g and the non-dimensional, reduced frequency k are defined as

$$g = \frac{\delta b}{W_0}, \quad k = \frac{\omega b}{W_0}, \tag{5}$$

https://doi.org/10.5194/wes-2026-9
Preprint. Discussion started: 10 February 2026

eawe european academy of wind energy
Open Access WIND ENERGY SCIENCE DISCUSSIONS

190 where the relative wind speed W_0 and profile half-chord length b have been used as reference lengths to non-dimensionalize the angular frequency ω and decay constant δ. Substituting Eq. 4 into Eq. 1 gives

$$\left(\frac{W_0^2}{b^2}p^2\mathbf{M}_\mathrm{s}+\frac{W_0}{b}p\mathbf{C}_\mathrm{s}+\mathbf{K}_\mathrm{s}\right)\hat{\mathbf{q}}=\frac{1}{2}\rho W_0^2\mathbf{A}(p,\alpha_0)\hat{\mathbf{q}},\ \text{with}\quad \mathbf{A}(p,\alpha_0)=\begin{bmatrix}F_{xx}(p,\alpha_0) & F_{xy}(p,\alpha_0) & F_{x\theta}(p,\alpha_0)\\ F_{yx}(p,\alpha_0) & F_{yy}(p,\alpha_0) & F_{y\theta}(p,\alpha_0)\\ M_{\theta x}(p,\alpha_0) & M_{\theta y}(p,\alpha_0) & M_{\theta\theta}(p,\alpha_0)\end{bmatrix}, \tag{6}$$

where the aerodynamic forces are defined as a 3x3 matrix with transfer functions mapping motion in each degree of freedom onto forces in each of the degrees of freedom. Eq. 6 is the well-known flutter equation which can be solved iteratively for 195 the eigenvalues p and the eigenvectors $\hat{\mathbf{q}}$, given the fact that the $\mathbf{A}$ matrix depends on p. For this system of three degrees of freedom, this results in three modes, for which the frequency and damping are defined by the eigenvalues and the modeshapes are defined by the eigenvectors. In this work, the g-method flutter solution procedure by Chen has been used, which proposes an approximation of the $\mathbf{A}(p,\alpha_0)$ matrix as a Taylor expansion along the imaginary axis, i.e. $\mathbf{A}(p,\alpha_0)\approx\mathbf{A}(\mathrm{i}k,\alpha_0)+g\mathbf{A}'(\mathrm{i}k,\alpha_0)$ (Chen, 2000). This allows to find frequency, damping and eigenvectors which are exact for damping equal to zero and a 200 good approximation for low damping values, but only requires the computation of the frequency domain aerodynamic forces $\mathbf{A}(\mathrm{i}k,\alpha_0)$. Note that only the first order harmonic forces are required, since the higher harmonic forces cancel out over one period in a sinusoidal motion.

2.2.1 High-fidelity frequency domain aerodynamic forces

The high-fidelity CFD frequency domain aerodynamic transfer functions are computed by a pulse identification method (Kaiser 205 et al., 2015). The basic idea is to do time domain simulations with a forced-motion pulse excitation, implying a broadband frequency excitation and allowing the determination of the full transfer functions for all forces. The practical procedure is to first compute the steady state equilibrium. Then, for each degree of freedom j, a time domain simulation is done with a pulse excitation p_j on that degree of freedom. In theory, this pulse signal should be infinitely small and infinitely short. For numerical reasons, the pulse has to be spread over a couple timesteps and the pulse amplitude is a compromise between being sufficiently 210 small, so the response is linear, and sufficiently large, such that it is not impacted by numerical errors. The transfer function onto degree of freedom i, caused by degree of freedom j can then be computed as

$$F_{ij}=\frac{2}{\rho W_0^2}\frac{\mathrm{FFT}\left(F_{i,\mathrm{pulsed}}-F_{i,\mathrm{undisturbed}}\right)}{\mathrm{FFT}\left(p_j\right)}. \tag{7}$$

To improve the numerical accuracy and to guarantee that only the linear response is captured, the forces from an undisturbed time domain simulation are subtracted from the pulsed result.

215 The DLR in-house tool Tau is used as CFD solver. The computational grid is shown in figure 3. It has a circular shape with a diameter of $400\,\mathrm{m}$ and a total of approximately $100\,000$ grid points. For all CFD results in this work, a RANS solver is used with a Spalart-Allmaras turbulence model. The sensitivity on the CFD methodology was tested by comparing with a k-ω

https://doi.org/10.5194/wes-2026-9
Preprint. Discussion started: 10 February 2026

turbulence model and with an inviscid Euler solution (on a different grid). The influence of the RANS turbulence model was negligible, the influence of ignoring viscosity small. The flow conditions were determined based on a relative inflow speed of $70\,\mathrm{m\,s^{-1}}$ under normal atmospheric conditions, resulting in a Reynolds number of 1.5×10^7 and a Mach number of 0.206.

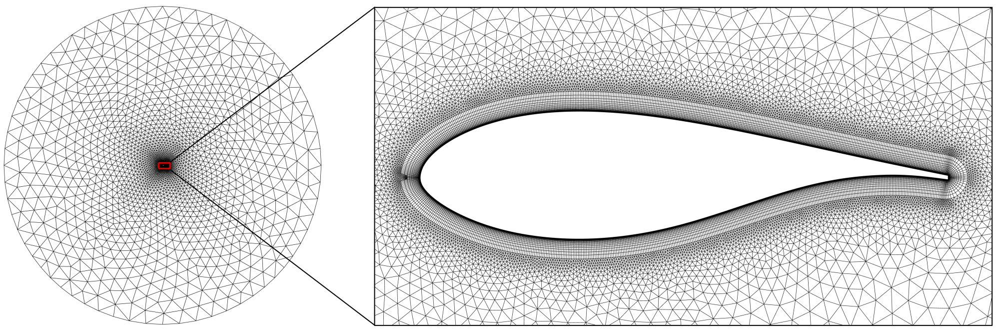

Figure 3. Overview and detail of the CFD Mesh

2.2.2 Low-fidelity frequency domain aerodynamic forces

The low-fidelity frequency domain aerodynamic model is derived based on a potential theory assumption. The transfer functions mapping harmonic motion in each of the degrees of freedom onto the first order harmonic forces in each of the degrees of freedom have to be found. As a first step, the forces in the direction of the degrees of freedom are given by the expressions

$$F_x(t) = L^{\mathrm{C}}(t)\sin\left(\alpha_{1/4}(t)\right) - D(t)\cos\left(\alpha_{1/4}(t)\right) \approx L^{\mathrm{C}}(t)\alpha_{1/4}(t) - D(t) \tag{8}$$

$$F_y(t) = L^{\mathrm{C}}(t)\cos\left(\alpha_{1/4}(t)\right) + L^{\mathrm{NC}}(t) + D(t)\sin\left(\alpha_{1/4}(t)\right) \approx L^{\mathrm{C}}(t) + L^{\mathrm{NC}}(t) + D(t)\alpha_{1/4}(t) \tag{9}$$

$$M_\theta(t) = M^{\mathrm{C}}(t) + M^{\mathrm{NC}}(t) + M_{\mathrm{camber}(t)} \tag{10}$$

as a function of aerodynamic forces; the circulatory lift L^{C}, the non-circulatory lift L^{NC}, the drag D, the angle of attack at the quarter chord point $\alpha_{1/4}$, the circulatory moment M^{C}, the non-circulatory moment M^{NC}, and the aerodynamic moment due to the airfoil camber M_{camber}. These expressions are consistent with the formulation presented by Li et al. (2022). Note that the non-circulatory lift L^{NC} is a normal force which acts perpendicular to the chord, so in y direction, and has no component in x direction. A further important point is that the direction of the aerodynamic force is defined by the angle of attack determined at the quarter chord point $\alpha_{1/4}$ and not by the angle of attack determined at the three quarter chord point, which should be used to compute the magnitude of the aerodynamic forces. In this work, the investigated angles of attack are small, so small angle approximations are used to drop the sines and cosines.

All components in Equations 8 - 10 are expanded in their time-invariant $(\bar{\cdot})$ and time-dependent $(\tilde{\cdot})$ parts. After reorganization, this gives

https://doi.org/10.5194/wes-2026-9
Preprint. Discussion started: 10 February 2026

$$F_x(t) = \underbrace{\overline{L}^{\mathrm{C}}\overline{\alpha}_{1/4} - \overline{D}}_{\text{Time-invariant mean}} + \overline{L}^{\mathrm{C}}\widetilde{\alpha}_{1/4} + \widetilde{L}^{\mathrm{C}}\overline{\alpha}_{1/4} - \widetilde{D} \tag{11}$$

$$F_y(t) = \underbrace{\overline{L}^{\mathrm{C}} + \cancel{\overline{L}^{\mathrm{NC}}} + \overline{D}\overline{\alpha}_{1/4}}_{\text{Time-invariant mean}} + \widetilde{L}^{\mathrm{C}} + \widetilde{L}^{\mathrm{NC}} + \overline{D}\widetilde{\alpha}_{1/4} + \widetilde{D}\overline{\alpha}_{1/4} \tag{12}$$

$$M_\theta(t) = \underbrace{\overline{M}^{\mathrm{C}} + \cancel{\overline{M}^{\mathrm{NC}}} + \overline{M}_{\text{camber}}}_{\text{Time-invariant mean}} + \widetilde{M}^{\mathrm{C}} + \widetilde{M}^{\mathrm{NC}} + \widetilde{M}_{\text{camber}} \tag{13}$$

To get the first order harmonic transfer functions of the forces, these equations have to be transformed into the frequency domain. Since the time-invariant parts do not contribute to these first order harmonic transfer functions, they are omitted, such that the expressions for the frequency domain forces become

$$F_x(k) = L^{\mathrm{C}}(k)\overline{\alpha}_{1/4} + \overline{L}^{\mathrm{C}}\alpha_{1/4}(k) - D(k) \tag{14}$$

$$F_y(k) = L^{\mathrm{C}}(k) + L^{\mathrm{NC}}(k)\left(+\overline{D}\alpha_{1/4}(k) + D(k)\overline{\alpha}_{1/4}\right) \tag{15}$$

$$M_\theta(k) = M^{\mathrm{C}}(k) + M^{\mathrm{NC}}(k) + M_{\text{camber}}(k) \tag{16}$$

These equations already show that the frequency domain force in x-direction has two main components. One component due to the frequency dependent circulatory lift projected with the mean angle of attack and one component due to the tilting of the steady lift vector caused by the frequency dependent variation of the angle of attack at the quarter chord point. Both viscous drag terms in the Eq. 15 are irrelevant compared to both lift components and are therefore ignored from here on forwards. To arrive at the individual transfer functions, the analytic description for each of the components in these equations has to be found.

The mean angles of attack are defined as

$$\overline{\alpha}_{1/4} = \alpha_0 = \arctan\left(\frac{V_0}{U_0}\right), \tag{17}$$

$$\alpha_{0,\text{eff}} = \alpha_0 - \alpha_{L=0}, \tag{18}$$

with the effective angle of attack $\alpha_{0,\text{eff}}$ including the zero lift angle of attack $\alpha_{L=0}$ for the cambered profile. The mean circulatory lift can then be computed as

$$\overline{L}^{\mathrm{C}} = \frac{1}{2}\rho W_0^2 2b C_{L_\alpha}\alpha_{0,\text{eff}}, \tag{19}$$

which includes effects due to the airfoil camber through both the tuned C_{L_α} and the effective angle of attack.

The expressions for the frequency dependent lift and moment can be derived based on the classical work by Theodorsen (1949) and Greenberg (1947). Theodorsen derives the frequency-dependent transfer functions for the unsteady aerodynamic

https://doi.org/10.5194/wes-2026-9
Preprint. Discussion started: 10 February 2026

lift and moment for the harmonic pitching and heaving motion of a flat plate. It includes the time lag effect due to shed vorticity by means of the complex Theodorsen function $C(k)$. The lift and moment components which are affected by the time lag due to shed vorticity and therefore include the Theodorsen function are called the circulatory forces. The lift and moment components which act instantaneously and represent the acceleration of the air around the airfoil are called the non-circulatory or apparent mass forces. The original Theodorsen function only includes translational motion perpendicular to the airstream. Greenberg (1947) extended this by including the effect of a time varying magnitude of the inflow, which can be reformulated to represent the effect of translational motion parallel to the airstream. Note that the Theodorsen and Greenberg expressions are derived for translational parallel and perpendicular to the airstream and not parallel and perpendicular to the chord. The Theodorsen and Greenberg expressions will therefore depend on x' and y' motion, as sketched in figure 1. The classic Theodorsen and Greenberg equations are given for time domain motion components which are transferred into the frequency domain by assuming harmonic motion with amplitude $\widehat{q}$ and reduced frequency k

$$\begin{aligned} q(t) &= && \widehat{q}e^{\frac{W_0}{b}\mathrm{i}kt}, \\ \dot{q}(t) &= \frac{W_0}{b}\mathrm{i}k && \widehat{q}e^{\frac{W_0}{b}\mathrm{i}kt}, \\ \ddot{q}(t) &= -\frac{W_0^2}{b^2}k^2 && \widehat{q}e^{\frac{W_0}{b}\mathrm{i}kt}, \end{aligned} \tag{20}$$

which gives the full expressions for the frequency domain circulatory and non-circulatory lift, as well as the circulatory and non-circulatory moment as

$$L^{\mathrm{C}}(k) = \frac{1}{2}\rho W_0^2 2C_{L_\alpha}\left[\underbrace{\left(-\mathrm{i}k\widehat{y'} + b\widehat{\theta} + \mathrm{i}kb\left(\frac{1}{2}-a\right)\widehat{\theta}\right)C(k)}_{\text{Theodorsen}} + \underbrace{\mathrm{i}k\alpha_{0,\mathrm{eff}}\left(1+C(k)\right)\widehat{x'}}_{\text{Greenberg terms}}\right] \tag{21}$$

$$L^{\mathrm{NC}}(k) = \frac{1}{2}\rho W_0^2 2\pi\left[\underbrace{k^2\widehat{y'} + \mathrm{i}kb\widehat{\theta} + k^2ba\widehat{\theta}}_{\text{Theodorsen}} \underbrace{-k^2\widehat{x'}\alpha_0}_{\text{Greenberg terms}}\right] \tag{22}$$

$$M^{\mathrm{C}}(k) = \frac{1}{2}\rho W_0^2 2C_{L_\alpha} b\left(\frac{1}{2}+a\right)\left[\underbrace{\left(-\mathrm{i}k\widehat{y'} + b\widehat{\theta} + \mathrm{i}kb\left(\frac{1}{2}-a\right)\widehat{\theta}\right)C(k)}_{\text{Theodorsen}} + \underbrace{\mathrm{i}k\alpha_{0,\mathrm{eff}}\left(1+C(k)\right)\widehat{x}}_{\text{Greenberg terms}}\right] \tag{23}$$

$$M^{\mathrm{NC}}(k) = \frac{1}{2}\rho W_0^2 2\pi\left[\underbrace{k^2ab\widehat{y'} + \mathrm{i}kb^2\left(\frac{1}{2}+a\right)\widehat{\theta} + k^2b^2\left(\frac{1}{8}+a^2\right)\widehat{\theta}}_{\text{Theodorsen}}\underbrace{-k^2ba\widehat{x'}\alpha_0}_{\text{Greenberg terms}}\right] \tag{24}$$

The Theodorsen and Greenberg formulations are derived for a flat-plate airfoil. However, the effect of the cambered airfoil can in parts be taken into account by using the actual profile-tuned C_{L_α} for the circulatory components, using the effective angle of attack for the circulatory Greenberg terms and by using the corrected aerodynamic center position.

https://doi.org/10.5194/wes-2026-9
Preprint. Discussion started: 10 February 2026

The time varying angle of attack at the quarter chord point is also derived starting from the expression for the unsteady angle of attack at the three quarter chord point by Theodorsen, but correcting for the distance between quarter and three quarter chord point, as also shown in Li et al. (2025). One additional effect has to be accounted for. If the typical section is to be a representation of an elastic structure, as is the case with a rotor blade, the coordinate systems defined in figure 1 should remain fixed in space for motion representing elastic deformations. To account for this effect, the relative motion of the coordinate system has to be subtracted. A more detailed explanation on this term is given in Appendix A. The final expression for the unsteady angle of attack at the quarter chord point is

$$\alpha_{1/4}(k) = \underbrace{\left(\widehat{\theta} - \frac{\mathrm{i}k}{b}\widehat{y}' + \left(\frac{1}{2} - a\right)\mathrm{i}k\widehat{\theta}\right)C(k)}_{\text{Theodorsen: } \alpha_{3/4}(k)} \underbrace{-\mathrm{i}k\widehat{\theta}}_{\text{Distance to } \alpha_{1/4}} \underbrace{-\widehat{\theta}.}_{\text{Fixed reference system}} \tag{25}$$

The additional pitching moment created by the cambered airfoil can be computed as

$$M_{\text{camber}} = C_{M_{\text{AC}}}\frac{1}{2}\rho W^2 2b \tag{26}$$

as a function of the pitching moment coefficient around the aerodynamic center $C_{M_{\text{AC}}}$. As this moment is a function of the relative wind speed, it also depends on the velocity of the section in x and y. Looking back at the velocity triangle in figure 1, the velocity term can be extended to

$$M_{\text{camber}} = C_{M_{\text{AC}}}\frac{1}{2}\rho 2b\left(U_0^2 + 2U_0\dot{x} + \dot{x}^2 + V_0^2 - 2V_0\dot{y} + \dot{y}^2\right), \quad U_0 = W_0\cos(\alpha_0) = W_0, \quad V_0 = W_0\sin(\alpha_0) = W_0\alpha_0. \tag{27}$$

Using small angle approximations, neglecting higher order terms, dropping the time-invariant part and again converting the velocity dependent terms into the frequency domain by applying Eq. 20 results finally in following expression for the unsteady frequency dependent moment due to the airfoil camber

$$M_{\text{camber}}(k) = \frac{1}{2}\rho W_0^2 C_{M_{\text{AC}}} 4\mathrm{i}k\hat{x} - \frac{1}{2}\rho W_0^2 C_{M_{\text{AC}}} 4\mathrm{i}k\alpha_0\hat{y} \tag{28}$$

The exact same procedure can be followed to obtain the expression for the unsteady drag force, but exchanging the pitching moment coefficient $C_{M_{\text{AC}}}$ with the drag coefficient C_{D_0}. Following the same steps, this gives

$$D(k) = \frac{1}{2}\rho W_0^2 C_{D_0} 4\mathrm{i}k\hat{x} + \frac{1}{2}\rho W_0^2 C_{D_0} 4\mathrm{i}k\alpha_0\hat{y}. \tag{29}$$

One final, somewhat special component is added to the low-fidelity aerodynamic description. Typically, the non-circulatory, apparent mass is only taken into account for motion normal to the chord. This term describes the inertial effect of the air surrounding the profile, when this profile is accelerated. The expression for the non-circulatory lift normal to the chord was given in 22, with the first term being the non-circulatory lift due to heave motion perpendicular to the chord. As the profile is relatively thick, the apparent mass effect was also noticeable in the CFD result for the edgewise F_{xx} term, this will be shown in section 3.1. The apparent mass parallel to the chord can be taken into account in an analogous manner to the apparent mass in the normal direction. The only difference is that, whereas the normal term depends on the square of the chord length, the chord-parallel term depends on the square of the thickness of the profile. This results in following expression for the non-circulatory force along the chord as a function of the relative thickness t^*

$$F_{xx}^{\mathrm{NC}}(k) = \frac{1}{2}\rho W_0^2 2\pi k^2 t^{*2}. \tag{30}$$

Inserting Equations 17, 19, 21, 22, 23, 24, and 25 into Equations 14, 15, and 16, normalizing with the dynamic pressure $\frac{1}{2}\rho W_0^2$, and gathering based on the separate components gives all aerodynamic transfer functions as a function of x', y', and θ.

$$F_{xx'}(k) = 2C_{L_\alpha}\left[\mathrm{i}k\alpha_{0,\mathrm{eff}} + \mathrm{i}k\alpha_{0,\mathrm{eff}}C(k)\right]\alpha_0 \tag{31}$$

$$F_{xy'}(k) = -2C_{L_\alpha}\mathrm{i}kC(k)\alpha_0 - 2C_{L_\alpha}\alpha_{0,\mathrm{eff}}\mathrm{i}kC(k) \tag{32}$$

$$F_{x\theta}(k) = 2C_{L_\alpha}\left[b + \mathrm{i}kb\left(\frac{1}{2}-a\right)\right]C(k)\alpha_0 + 2bC_{L_\alpha}\alpha_{0,\mathrm{eff}}\left[\left(1+\left(\frac{1}{2}-a\right)\mathrm{i}k\right)C(k) - \mathrm{i}k - 1\right] \tag{33}$$

$$F_{yx'}(k) = 2C_{L_\alpha}\left[\mathrm{i}k\alpha_{0,\mathrm{eff}} + \mathrm{i}k\alpha_{0,\mathrm{eff}}C(k)\right] - 2\pi k^2\alpha_0 \tag{34}$$

$$F_{yy'}(k) = -2C_{L_\alpha}\mathrm{i}kC(k) + 2\pi k^2\left(-C_{D_0}2\mathrm{i}kC(k)\right) \tag{35}$$

$$F_{y\theta}(k) = 2C_{L_\alpha}\left[b + \mathrm{i}kb\left(\frac{1}{2}-a\right)\right]C(k) + 2\pi\left[\mathrm{i}kb + k^2ba\right]\left(+C_{D_0}2b\left[\left(1+\left(\frac{1}{2}-a\right)\mathrm{i}k\right)C(k) - \mathrm{i}k - 1\right]\right) \tag{36}$$

$$M_{\theta x'}(k) = 2C_{L_\alpha}b^2\left(\frac{1}{2}+a\right)\left[\alpha_0\frac{\mathrm{i}k}{b} + \alpha_0\frac{\mathrm{i}k}{b}C(k)\right] - 2\pi k^2ba\alpha_0 \tag{37}$$

$$M_{\theta y'}(k) = -2C_{L_\alpha}b\left(\frac{1}{2}+a\right)\mathrm{i}kC(k) + 2\pi k^2ab \tag{38}$$

$$M_{\theta\theta}(k) = 2C_{L_\alpha}b^2\left(\frac{1}{2}+a\right)\left[1+\left(\frac{1}{2}-a\right)\mathrm{i}k\right]C(k) + 2\pi\left[-\mathrm{i}kb^2\left(\frac{1}{2}-a\right) + k^2b^2\left(\frac{1}{8}+a^2\right)\right] \tag{39}$$

The final transfer functions depending on x, y, and θ can be assembled by rotating the transfer functions depending on x' and y' with the steady angle of attack and by adding the moment and drag components of equations 28, 29, and 30 resulting in

$$\mathbf{A}(k,\alpha_0) = \begin{bmatrix} F_{xx'}(k) & F_{xy'}(k) & F_{x\theta}(k) \\ F_{yx'}(k) & F_{yy'}(k) & F_{y\theta}(k) \\ M_{\theta x'}(k) & M_{\theta y'}(k) & M_{\theta\theta}(k) \end{bmatrix} \begin{bmatrix} \cos\alpha_0 & -\sin\alpha_0 & 0 \\ \sin\alpha_0 & \cos\alpha_0 & 0 \\ 0 & 0 & 1 \end{bmatrix} + \begin{bmatrix} C_{D_0}4\mathrm{i}k + 2\pi k^2 t^{*2} & C_{D_0}4\mathrm{i}k\alpha_0 & 0 \\ 0 & 0 & 0 \\ C_{M_{\mathrm{AC}}}4\mathrm{i}k & C_{M_{\mathrm{AC}}}4\mathrm{i}k\alpha_0 & 0 \end{bmatrix}. \tag{40}$$

2.3 Summary and corrections methodology Stäblein et al. (2017a)

The methodology presented in Stäblein et al. (2017a) is used as literature reference result. The methodology relies on a linearization of the aerodynamic model, transforming the system in a linear state-space system. This methodology is based on the work by Hansen (2004), but the implementation used for the analysis in Stäblein et al. (2017a) was a standalone code. The detailed derivation of the methodology is not repeated here, but the comparison carried out in process of this work revealed a couple mistakes and modeling differences in Stäblein et al. (2017a). These points are listed here and an updated python implementation of the state-space model is available on Github[1].

Incorrect implementation of steady lift computation: The first point is a mistake in the computation of the steady lift (Stäblein et al. (2017a), Eq. 16). The code implementation did not include the chord term c, which means that the steady lift was underestimated with a factor of 3.292, the chord length of the investigated section. Furthermore, the influence of the zero-lift angle of attack of approximately $-3°$ was not taken into account, leading to a further underestimation of the steady lift. The underestimation of the lift has a significant influence on the stability of the edgewise mode.

Definition of the reference system: The second point is the definition of the degrees of freedom. As explained previously and elaborated in Appendix A, the definition of the reference frame either moving with the profile or remaining fixed in space is important. Stäblein et al. used a moving reference system, and therefore the typical section rather represents a flight-mechanical system, than an elastic system.

Angle of attack for lift force direction: The third point is the definition of the induced drag due to the lagging of the effective angle of attack behind the geometric angle of attack. The formulation by Stäblein et al. uses the angle of attack computed at the three-quarter chord point (Stäblein et al. (2017a), Eq. 11 and 19), and not the angle of attack at the quarter chord point, as proposed by Li et al. (2025). This resulted in a significant difference in the imaginary part of the $F_{x\theta}$ force with the CFD reference result, which also had a slight influence on edgewise damping and the edgewise instability point.

Non-circulatory lift as normal force: The fourth point is the non-circulatory lift. As discussed in Li et al. (2025), the non-circulatory lift is a normal force, which should therefore only have a component in y direction. Stäblein et al. applied the non-circulatory lift in the lift direction perpendicular to the relative wind, therefore inducing a component in x direction. This resulted in a significantly poorer agreement with the CFD reference result for the real part of F_{xx} and F_{xy}. The influence on the edgewise damping and flutter point was relatively small.

Definition of the torsional stiffness: Finally, the torsional stiffness was defined as $k_\theta = J\omega_\theta^2$, with J representing the rotational inertia around the center of gravity and with the uncoupled torsional frequency ω_θ. The structural stiffness should have been defined with the rotational inertia around the elastic axis. This correction results in a slightly lower torsional frequency.

It is interesting to notice that the verification of the methodology and implementation performed in Stäblein et al. (2017a) did not uncover these mistakes. The verification exercise involved comparing the flutter speed of a classical flutter mechanism, calculated for various structural properties of the blade section, against literature reference data. Only classical flutter reference data was available. This explains why most of these mistakes were not uncovered, and already shows how the classical flap-twist flutter mechanism and edgewise flutter mechanism have different sensitivities.

[1]https://github.com/DLR-AE/jfs_2016, if this paper gets accepted as corrigendum, this fork can be merged into the original repository.

https://doi.org/10.5194/wes-2026-9
Preprint. Discussion started: 10 February 2026

3 Influence of the aerodynamic modeling on the edge-twist flutter prediction

In this section, the stability results for all three methods are compared to show whether there are any noticeable qualitative or quantitative differences between them. First, the frequency domain aerodynamic forces are compared directly, then the overall flutter behavior as a function of the edge-twist and flap-twist structural coupling, as well as of the steady angle of attack is shown, and finally the results of the flutter analysis are shown in more detail for a selected number of cases.

3.1 Frequency domain aerodynamic forces

The frequency domain aerodynamic transfer functions of the matrix $\mathbf{A}$ in Eq. 6 can be compared directly to identify possible differences in the aerodynamic modeling. The formulation in Stäblein et al. (2017a) does not explicitly require the aerodynamic transfer functions, so they are not derived in detail. To allow a direct comparison, the transfer functions are identified from the state-space system of the aerodynamic forces in Stäblein et al. (2017a). This approach is verified by using these identified transfer functions in a frequency domain flutter analysis with the method as explained in section 2.2. The stability analysis results showed a negligible difference with respect to the results obtained with the standard approach shown in Stäblein et al. (2017a), ensuring that the transfer functions correctly represent the aerodynamic model implementation. In figure 4, the aerodynamic transfer functions are compared directly in terms of their real and imaginary part with respect to the reduced frequency k. This figure has the same structure as the matrix $\mathbf{A}$. The pictograms in the top left corner give an indication which combination of input motion and induced force component the transfer function represents. The first column are the forces induced by edgewise motion, the middle column are the forces induced by flapwise motion, and the last column are the forces induced by torsional motion. In the other direction, the first row are the forces acting in edgewise direction, the second row are the forces acting in flapwise direction and the bottom row are the aerodynamic moments acting around the elastic axis. The transfer functions may be expressed in magnitude-phase form, but examining their real and imaginary parts is more effective for identifying limitations in the low-fidelity aerodynamic models, as it is often possible to directly relate the components of the transfer functions to specific terms in the low-fidelity aerodynamic formulations. Predominantly, the real parts of the transfer functions correspond to displacement or acceleration terms in the aerodynamic formulations, imaginary parts correspond to velocity-dependent terms. However, unsteady aerodynamic effects create time lags and therefore results in a mixing of real and imaginary parts by means of the complex Theodorsen function. The transfer functions are shown here up to a reduced frequency of $k = 1$, but for the system and relative wind speeds shown in this study, the lower reduced frequencies, up to $k = 0.3$, are most relevant for the stability analysis. Overall, a good agreement between the high-fidelity CFD reference result and both low-fidelity results can be seen. This is especially true for the transfer functions with the highest magnitude and therefore also likely a higher sensitivity towards the stability of the system. Following paragraphs give a more detailed discussion for the individual transfer functions.

Classical Theodorsen components F_{yy}, $F_{y\theta}$, $F_{\theta y}$, $F_{\theta\theta}$: These are the transfer functions describing the forces induced by and working on flapping motion and torsional motion. Both low-fidelity methodologies match well with the high-fidelity result.

https://doi.org/10.5194/wes-2026-9
Preprint. Discussion started: 10 February 2026

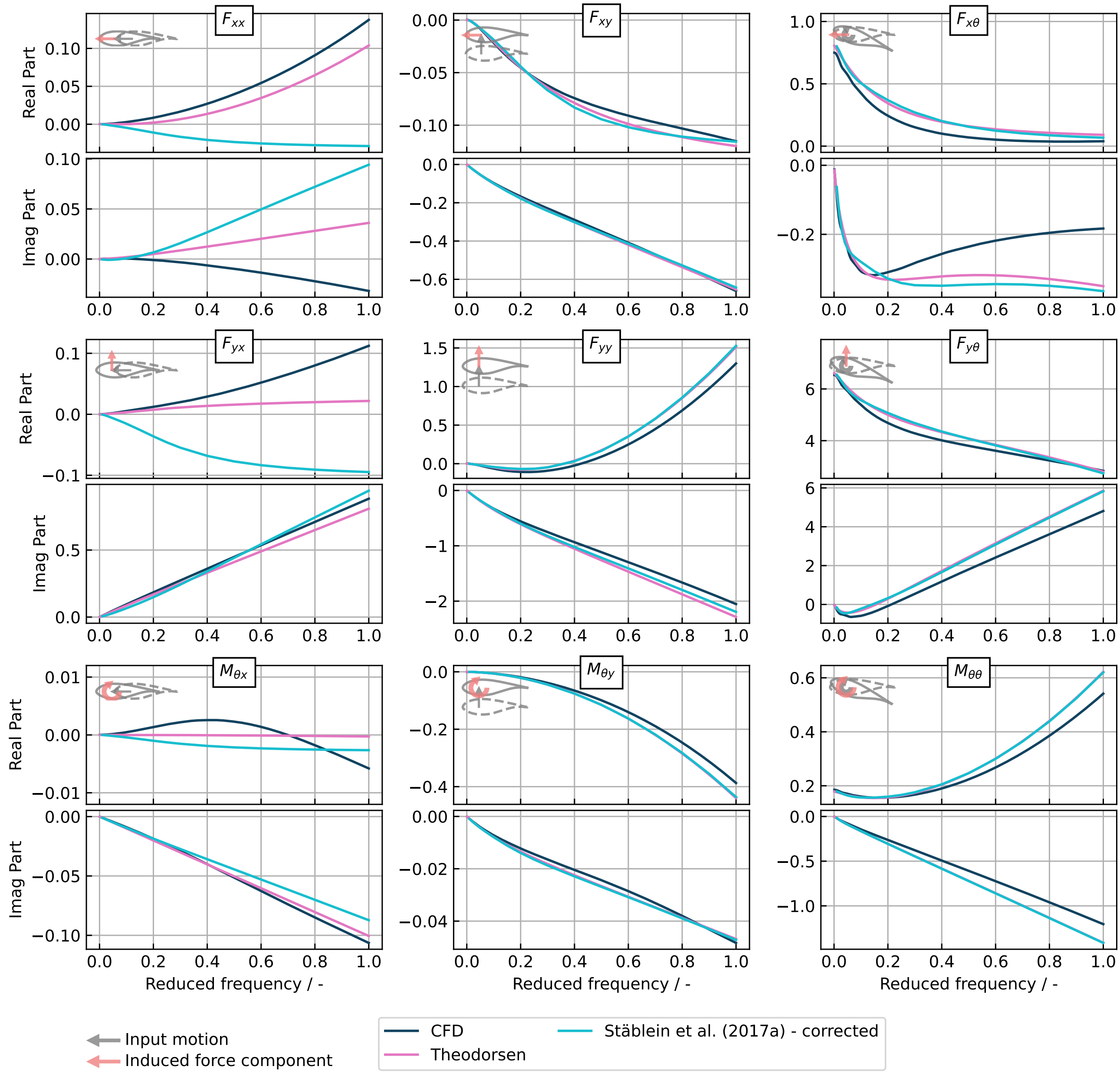

Figure 4. Comparison of the frequency domain transfer functions of the A-matrix from Eq. 6 determined by the high-fidelity CFD approach, the low-fidelity Theodorsen based approach and the corrected literature reference

An even better agreement was found for a comparison with a thin, uncambered NACA 0006 profile. The remaining differences are therefore likely attributable to the camber and thickness of the profile. In the Stäblein et al. (2017a) implementation, the Jones constants in the unsteady aerodynamic formulation could be tuned to improve the agreement of these terms. However,

https://doi.org/10.5194/wes-2026-9
Preprint. Discussion started: 10 February 2026

in an attempt to optimize these constants, a noticeable improvement could be achieved for these terms, but this went together with a poorer match for some other terms. Therefore it was decided to stick with the flat-plate Jones constants. Finally, note the high relevance of these components relative to the other components, as shown by the relatively high magnitudes of these transfer functions.

Edgewise force induced by pitching motion $\boldsymbol{F_{x\theta}}$: This function is strongly affected by the definition of a fixed or body-fixed reference system as discussed in appendix A. This transfer function shows overall a combination of two effects, the variation of the magnitude of the lift component projected in x-direction and the variation of the projection of the steady lift vector in x-direction due to the variation of the unsteady angle of attack. The real part shows a satisfying agreement between the different methods. A notable discrepancy exists between the CFD and both low-fidelity results in the imaginary component. This term, which is mostly affected by the pitch velocity, is highly sensitive to the choice of the chordwise position where the angle of attack is computed to determine the direction of the steady lift vector. As discussed before, the angle of attack at the 1/4-chord point should be used in this case, as presented in Li et al. (2025). Not shown here, but using the 3/4-chord point for the angle-of-attack determination results in a significantly poorer agreement. The remaining discrepancy, particularly at higher reduced frequencies, remains unexplained.

Edgewise force induced by flapwise motion $\boldsymbol{F_{xy}}$: This component is primarily defined by the flapwise velocity creating an apparent angle of attack. Again, the apparent angle of attack will influence both the magnitude of the lift component projected in the x-direction and the unsteady variation of the direction of the steady lift vector. All three methods are in excellent agreement for both the real and imaginary part.

Edgewise force induced by edgewise motion $\boldsymbol{F_{xx}}$: In the real part, a significant difference exists between the CFD and low-fidelity Theodorsen methodology on one hand, and the Stäblein formulation on the other hand. This difference is almost exclusively the added mass effect due to the relatively thick airfoil, included in the low-fidelity Theodorsen implementation with Eq. 30. This difference has a big impact on this transfer function, but its influence on the stability result is small. There is a poor agreement between the different methods in the imaginary part, with the CFD and low-fidelity methods even showing opposite signs. A definitive explanation for this discrepancy has not been identified. However, it is likely that some of the flow physics related to the forces induced by edgewise motion are not captured by the low-fidelity models.

Flapwise force induced by edgewise motion $\boldsymbol{F_{yx}}$: This transfer function is dominated by the edgewise velocity term, as the section's edgewise velocity directly scales the lift magnitude, and consequently the flapwise force. Both the low-fidelity Theodorsen methodology, via the Greenberg terms, and the Stäblein methodology correctly capture this, illustrated by the excellent agreement in the imaginary component. The real part has a significantly smaller amplitude. The CFD and low-fidelity Theodorsen result have the same sign and trend, but deviate significantly at higher reduced frequencies. The Stäblein implementation deviates both in sign and trend.

Pitching moment induced by edgewise motion $\boldsymbol{M_{\theta x}}$: Equivalent to F_{yx}, the imaginary part is most dominant, due to the direct scaling of the pitching moment with the edgewise velocity. The trends in the real part do not agree between the tools, but the amplitude of this component is small relative to the imaginary part and relative to the other transfer functions.

https://doi.org/10.5194/wes-2026-9
Preprint. Discussion started: 10 February 2026

Altogether, this comparison of the frequency domain transfer functions shows that the low-fidelity methodologies agree well with the CFD reference result for the terms with the highest amplitudes, while some differences remain in some of the components induced by or acting in edgewise direction.

3.2 Overview: Influence of structural coupling and operating point

The stability of a wind turbine blade section, especially the edgewise damping and edgewise instability mechanisms, depends strongly on the structural edge-twist and flap-twist coupling, as shown in Stäblein et al. (2017a). Besides this, it also depends significantly on the steady angle of attack, as shown in Stäblein et al. (2017b). This section shows the overall stability characteristics of the blade section for variations in the structural edge-twist coupling parameter γ_x and flap-twist coupling parameter γ_y, in both cases within relevant ranges for large and flexible wind turbine blades. The stability analysis is done for a steady angle of attack of $0°$ and $7°$ by fixing the steady angle of attack and stepwise increasing the relative wind speed. A critical inflow speed is identified as the lowest wind speed at which one of three modes of the system either has a negative damping or diverges. The resulting instabilities are categorized into three groups. Classical flutter implies that the damping of either the flapwise or torsional modes is negative. Edgewise flutter implies that the damping of the edgewise modes is negative. Divergence implies that for one of the modes the frequency fell to zero and the damping to increased to infinity.

Figure 5 shows for all three methods the critical inflow speed at which the blade section becomes dynamically unstable or diverges and the type of instability which occurs when both structural coupling parameters are varied independently. The plots on the left only vary the edge-twist coupling with zero flap-twist coupling, the plots on the right vary the flap-twist coupling with zero edge-twist coupling. The results of both low-fidelity methodologies agree well with the CFD reference result. Overall, the parameter dependencies align with those reported in Stäblein et al. (2017a), though there are some key differences. Structural edge-twist coupling in both the edge-twist to feather and edge-twist to stall direction leads to a strong reduction in the critical inflow speed. In contrast with the original result in Stäblein et al. (2017a), the edgewise flutter boundary is not symmetric with respect to the edge-twist coupling. The flutter boundaries in edge-twist to feather and edge-twist to stall direction also depend differently on the steady angle of attack. For an edge-twist coupling to feather the critical inflow speed increases with the steady angle of attack, for edge-twist coupling to stall the opposite effect is apparent. The critical inflow speed drops significantly with increasing steady angle of attack. The critical inflow speed for a classical flutter mechanism is largely unaffected by the edge-twist coupling parameter, and for most of the edge-twist coupling range, it is significantly higher than the critical inflow speed for edgewise flutter. The plots on the right show that there is no edgewise flutter mechanism without edge-twist coupling. The critical inflow speed for the classical flutter mechanism reduces slightly with flap-twist coupling to feather, but stays close to or above $200\,\mathrm{m\,s^{-1}}$. With increasing flap-twist coupling to stall the divergence boundary drops steeply. There is no noticeable difference between the right-hand side plots in figures 5a and 5b, illustrating that the steady load has no significant influence on the sensitivity of the flap-twist coupling.

Figures 6 and 7 show the critical inflow speed for a combined variation of the structural edge-twist and flap-twist coupling at a steady angle of attack of $7°$ and $0°$, respectively. Again, the overall results for all three methods are in satisfying agreement, with a slightly better match between the CFD and Theodorsen results. Most findings made based on the independent variations

https://doi.org/10.5194/wes-2026-9
Preprint. Discussion started: 10 February 2026

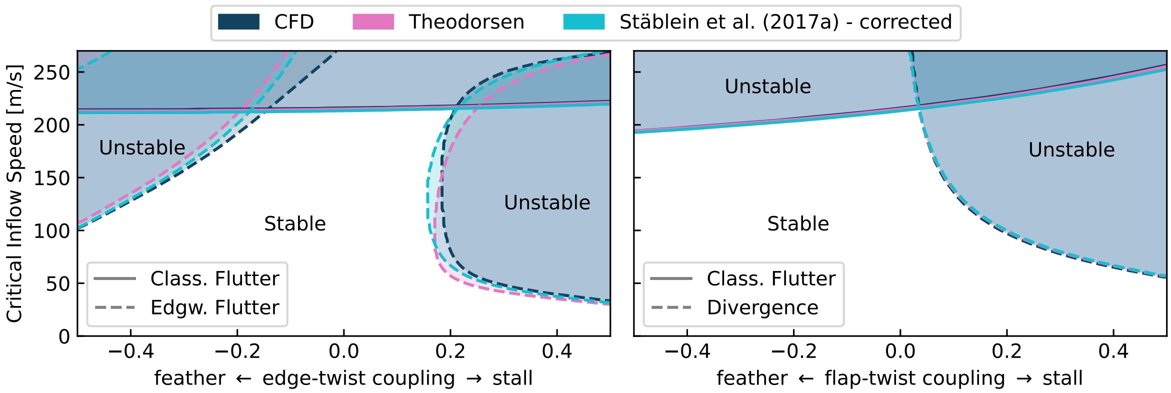

(a) Steady angle of attack 7°

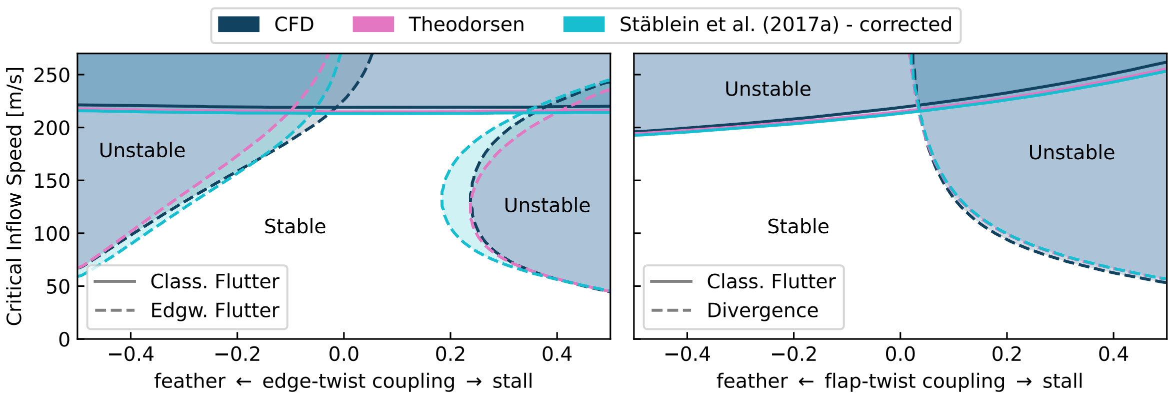

(b) Steady angle of attack 0°

Figure 5. Effect of individual variations in structural edge-twist and flap-twist coupling on the critical inflow speed of the blade section

of the coupling terms remain. Structural flap-twist coupling to stall results in a divergent system. A system with flap-twist coupling to feather results either in classical flutter, when the edge-twist coupling is between approximately 0 and 0.2, or edge-twist flutter when there is sufficient edge-twist coupling in either direction. Note that the independent variation case shown on the left of figure 5 without any flap-twist coupling is non-conservative. This figure corresponds to the vertical slice at flap-twist coupling = 0 in figures 6 and 7. The critical inflow speeds for edge-twist flutter drop significantly when including flap-twist coupling to feather, and therefore moving further to the left in the diagram.

In the upcoming sections the stability characteristics of the blade section will be investigated in closer detail based on six cases. It is decided to only analyze points with flap-twist coupling to feather, which are more relevant for real wind turbine designs. In the six selected cases the edge-twist coupling is varied between -0.3, 0, and 0.3 and the flap-twist coupling is varied

https://doi.org/10.5194/wes-2026-9
Preprint. Discussion started: 10 February 2026

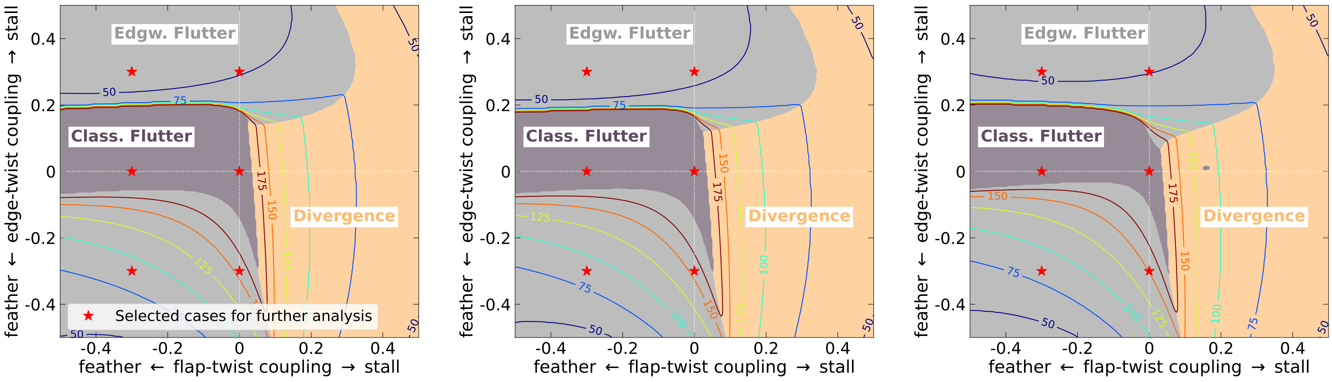

(a) CFD (b) Theodorsen (c) Stäblein et al. (2017a) - corrected

Figure 6. Effect of combined variations in structural edge-twist and flap-twist coupling on the critical inflow speed of the blade section at a steady angle of attack of 7°

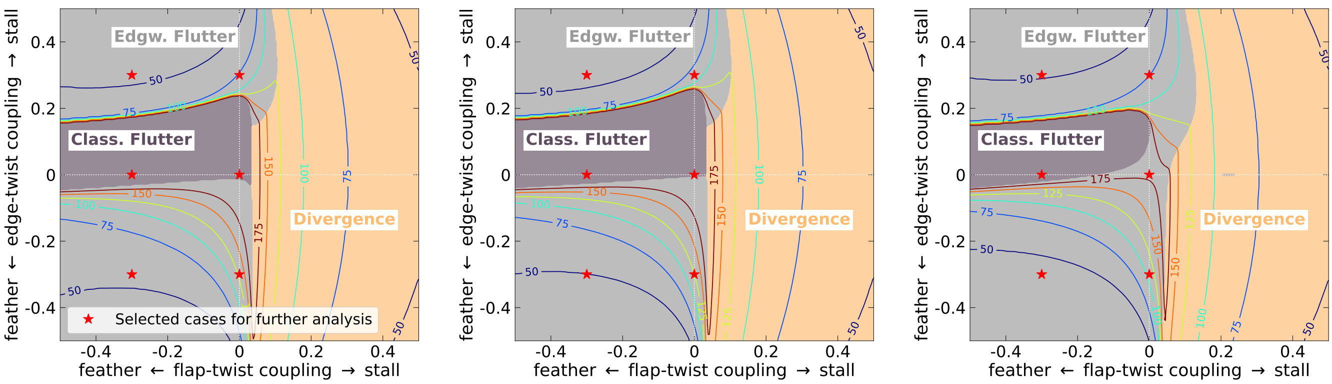

(a) CFD (b) Theodorsen (c) Stäblein et al. (2017a) - corrected

Figure 7. Effect of combined variations in structural edge-twist and flap-twist coupling on the critical inflow speed of the blade section at a steady angle of attack of 0°

between -0.3 and 0. These design points are meaningful and relevant for current and future designs. The selected points are highlighted with the red markers in figures 6 and 7.

3.3 Flutter analysis: Influence of structural coupling and operating point

This section presents further analysis of the six cases selected in section 3.2, which are also highlighted in figures 6 and 7. The flutter analysis conducted on these cases will be used to highlight trends and characteristics of modal frequency and damping as a function of relative wind speed.

https://doi.org/10.5194/wes-2026-9
Preprint. Discussion started: 10 February 2026

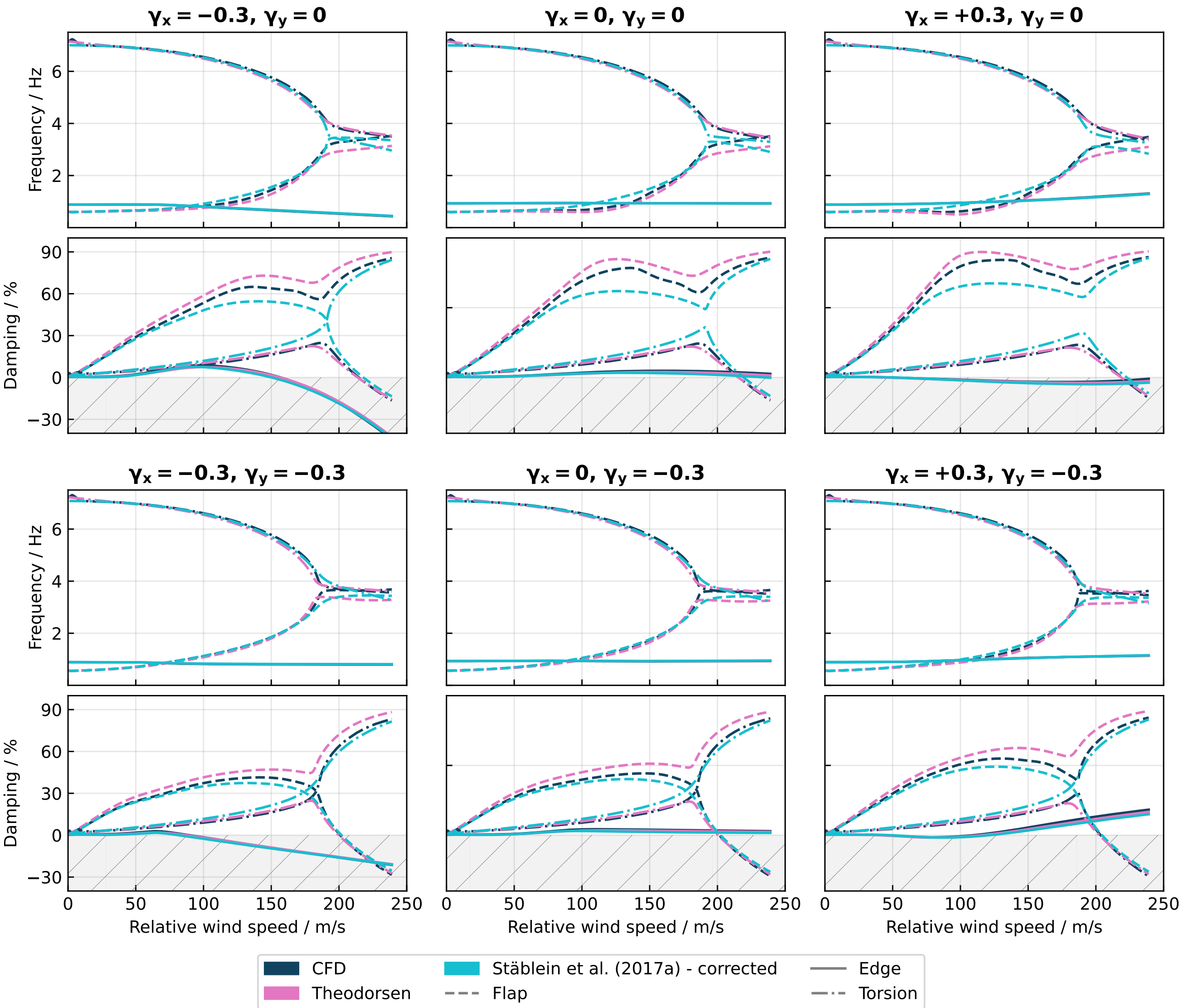

Figure 8. Frequency and damping of the three modes for the six selected cases at a steady angle of attack of 7°

Figure 8 compares the flutter analysis results across all three methods for the six selected cases at a steady angle of attack of 7°. The first row shows results without flap-twist coupling, while the second row presents results with flap-twist coupling to feather. These flutter diagrams depict the frequency and damping of the system's three modes as a function of relative wind speed. A clear classical flap-twist flutter coupling is observed in all cases. Specifically, the frequency of the lower frequency flap mode increases, while the frequency of the higher-frequency torsional mode decreases, causing the two modes to almost coalesce around $200\,\mathrm{m\,s^{-1}}$. This coupling results in a steep drop in the damping of one mode, while the damping of the other

mode sharply increases. The frequency and damping of both the flap and torsional modes remain relatively unchanged with variations in γ_x. However, for variations in γ_y, both the damping trends and the flutter points of these modes show slight changes. The results from all three methods are in strong agreement regarding the frequency and damping of the flap and torsional modes. A qualitative difference is observed in the damping of the highly-damped flapwise mode. This is expected, as the flutter analysis using the g-method is exact only for small damping values, and is only an approximation for higher damping
495 levels.

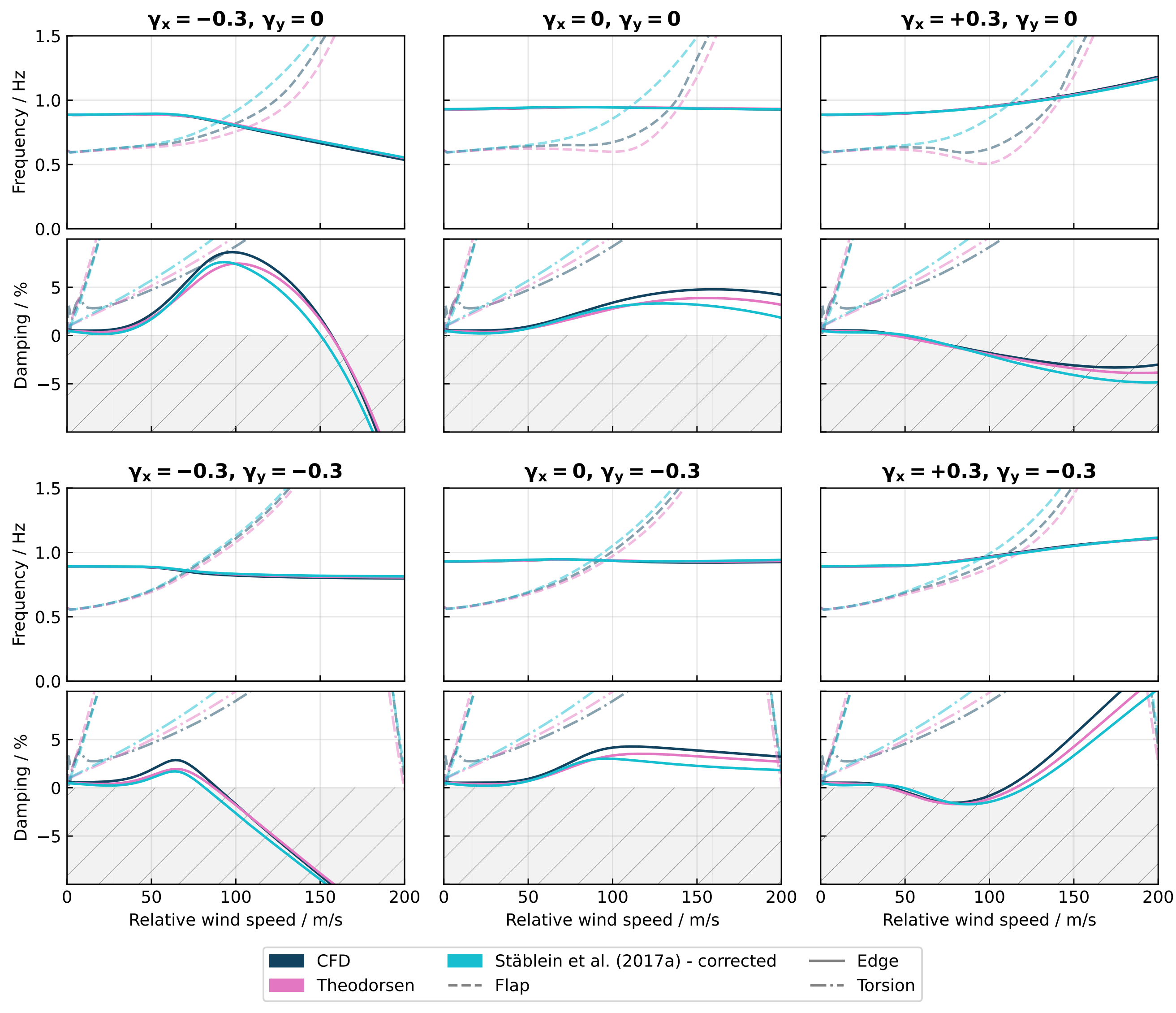

Figure 9. Detailed focus on the frequency and damping of the edgewise mode for the six selected cases at a steady angle of attack of 7°

https://doi.org/10.5194/wes-2026-9
Preprint. Discussion started: 10 February 2026

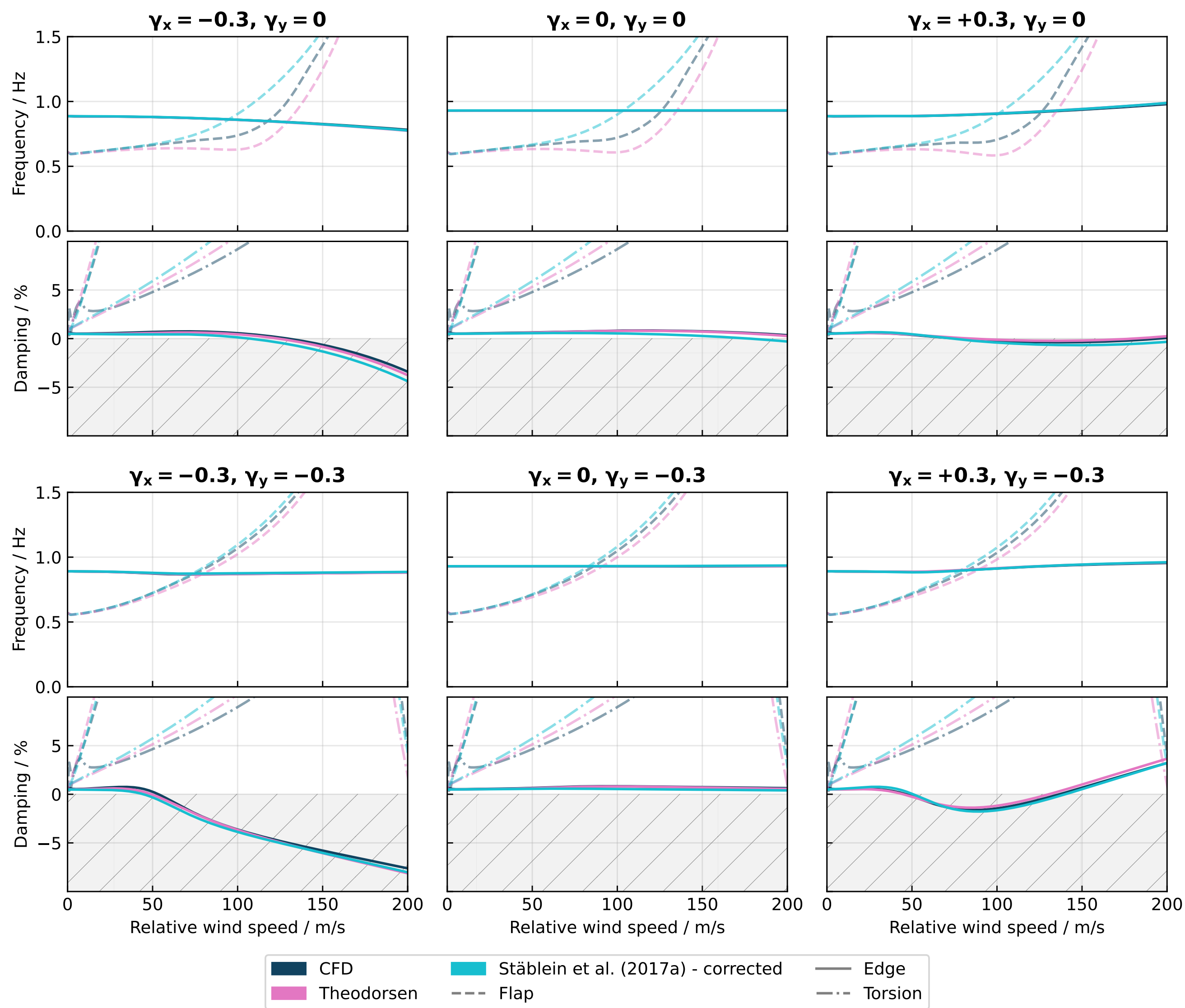

Figure 10. Detailed focus on the frequency and damping of the edgewise mode for the six selected cases at a steady angle of attack of 0°

The edgewise mode does not explicitly couple with the other modes in the same way as the torsional and flapwise modes do in classical flutter. The changes in frequency and damping of the edgewise mode are less pronounced compared to those of the flapwise and torsional modes. Nevertheless, the edgewise mode becomes unstable. As shown in section 3.2, the critical instability point for the edgewise mode occurs at a much lower relative wind speed than that of the classical flutter mechanism, provided there is sufficient structural edge-twist coupling. Later, section 5 will further investigate the reasons for the trends observed in the edgewise mode. The primary focus of this study is the damping prediction of the edgewise mode and the

https://doi.org/10.5194/wes-2026-9
Preprint. Discussion started: 10 February 2026

investigation of the edge-twist flutter mechanism. Therefore, Figure 9 presents a zoomed-in version of the flutter analysis for a steady angle of attack of 7°, with an emphasis on the edgewise mode. The first row of this figure shows results without flap-twist coupling. In the absence of edge-twist coupling (middle column), there is no instability up to a relative wind speed of $240\,\mathrm{m\,s^{-1}}$. With edge-twist coupling to feather, damping initially increases sharply, but then decreases rapidly at higher wind speeds, with a critical flutter point around $150\,\mathrm{m\,s^{-1}}$. With edge-twist coupling to stall, the damping is much lower overall, and the critical flutter speed is very low, occurring at approximately $50\,\mathrm{m\,s^{-1}}$, marked by a shallow transition into negative damping. The modal frequency remains nearly constant up to $80\,\mathrm{m\,s^{-1}}$, then decreases linearly for edge-twist coupling to feather, or increases linearly for edge-twist coupling to stall. In the second row, which includes flap-twist coupling to feather, it is observed that while some trends remain similar, significant differences emerge compared to the first row. With edge-twist coupling to feather, damping still increases initially, but the drop in damping occurs much earlier, resulting in a lower critical flutter speed. For edge-twist coupling to stall, the initial trends remain similar: damping decreases with relative wind speed, and the critical flutter speed is very low, characterized by a shallow crossing into negative damping. Flap-twist coupling causes the damping to increase again, and the blade section stabilizes after approximately $120\,\mathrm{m\,s^{-1}}$.

Figure 10 shows the flutter analysis results for the same structural coupling values but at a steady angle of attack of 0°. Comparing these results with those at 7° in figure 9 reveals that while most trends remain consistent, the variation in frequency and damping with respect to relative wind speed is less pronounced at 0°.

Finally, comparing the flutter analysis results for the edgewise mode across the three methods, shown in figures 9 and 10, reveals only minor qualitative differences. The modal frequencies are consistent across methods, with slight differences in damping and flutter points, particularly between the corrected literature result and the CFD reference result.

4 Sensitivity analysis of aerodynamic model components on stability predictions

The overviews shown in the contour plots in section 3.2 and the more detailed look into the flutter diagrams in section 3.3 have shown that the differences between the high-fidelity CFD reference result and both low-fidelity methodologies are small. These comparisons did not yet uncover which specific aspects in the low-fidelity aerodynamic model have the biggest impact on the final stability result. The goal of this section is therefore to show which specific terms in the aerodynamic model have the highest sensitivity towards the damping of the edgewise mode and the edgewise instability. The viscous CFD RANS result remains the reference result. The full Theodorsen result is repeated as the baseline for most model modifications. An overview of the different model modifications which are compared is given in Table 3. The influence of these modifications on the frequency domain aerodynamic forces is discussed in the table and shown in figure 11.

Figure 12 shows the frequency and damping of the edgewise mode for the different aerodynamic model modifications for the four selected cases which showed an edgewise instability. The analysis of these results reveals varying sensitivities of the stability outcomes to each modification, with some changes having a surprisingly large impact, while others exhibit minimal influence.

Table 3. Overview of the different model modifications which are compared in the sensitivity study

Model	Description
CFD	Viscous CFD RANS reference result
CFD - inviscid	Inviscid CFD, computed with an Euler solver. Note that a different computational grid, optimized for the Euler solver, was used instead of the one shown in figure 3.
Theodorsen	Full low-fidelity baseline result, as introduced in section 2.2.2
Theodorsen - without edgewise induced forces	Theodorsen aerodynamic forces, but forces induced by edgewise motion are omitted. As can be seen in figure 11, the full first column of the aerodynamic forces is zero.
Theodorsen - without pitching moment	Theodorsen aerodynamic forces, but all pitching moments are omitted. As can be seen in figure 11, the full last row of the aerodynamic forces is zero.
Theodorsen - without non-circulatory forces	Theodorsen aerodynamic forces, but all non-circulatory terms are disabled. The effect on the aerodynamic forces in figure 11 is most pronounced in the real parts of F_{yy}, $F_{y\theta}$, $M_{\theta y}$, $F_{\theta\theta}$ and in the imaginary part of $F_{y\theta}$.
Theodorsen - without steady load	Theodorsen aerodynamic forces, but the steady load vector is set to zero, which is apparent in the transfer functions of the edgewise forces F_{xx}, F_{xy}, and $F_{x\theta}$.
Quasi-steady	Theodorsen aerodynamic forces, but the unsteady lag-effect is eliminated by setting the Theodorsen function $C(k)$ to 1

The modification that demonstrates the highest sensitivity is the omission of the effect of the steady load on the unsteady aerodynamic forces. As shown in figure 12, which shows the case at 7° angle of attack, this modification significantly alters both the quantitative damping and the qualitative trends. This illustrates the critical role that steady loads play in the stability analysis which highlights the importance of incorporating steady aerodynamic effects.

Eliminating the forces induced by edgewise motion also leads to a noticeable change in the stability results. Although the qualitative trends in damping remain similar, both the flutter point and the quantitative damping values differ substantially, as seen in figure 12.

In contrast, several other modifications reveal minimal sensitivity, with the stability results remaining largely unchanged compared to the CFD and Theodorsen baseline results. For instance, the use of an inviscid assumption in the modified CFD model does not substantially alter the stability results compared to the viscous reference CFD case. This outcome can be explained by the high Reynolds number operating conditions of the blade section considered in this study, where the influence of viscosity is relatively small. It is also noteworthy that the stability results from the inviscid CFD model do not converge

https://doi.org/10.5194/wes-2026-9
Preprint. Discussion started: 10 February 2026

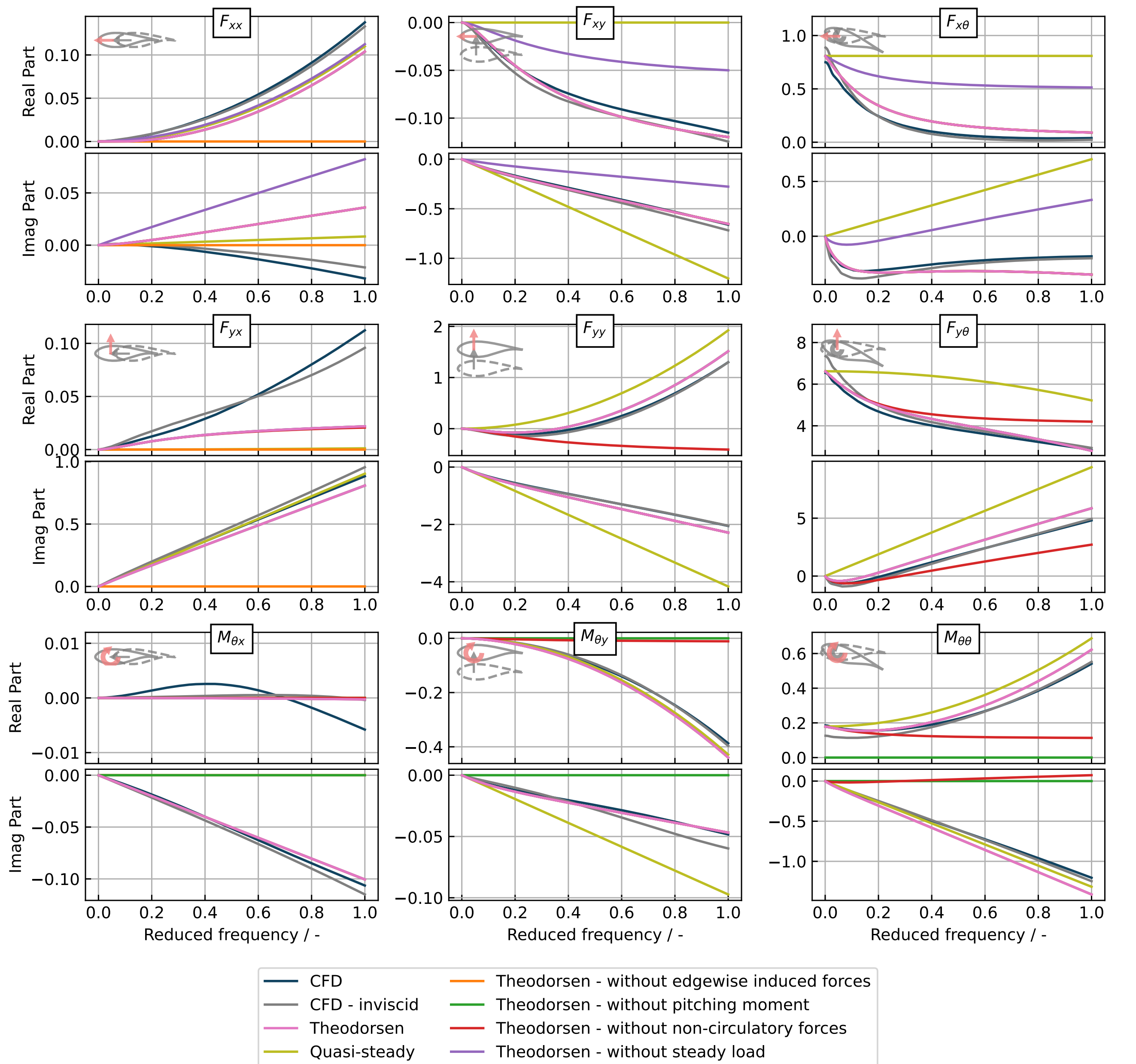

Figure 11. Sensitivity of the frequency domain aerodynamic forces for different modifications of the aerodynamic models. The modifications are summarized in Table 3.

towards the Theodorsen model result, despite the latter's inherent assumption of inviscid flow. This discrepancy is likely due to the fact that the Theodorsen model was tuned using steady viscous CFD results, such as the lift curve slope C_{L_α}, which leads to a less direct comparison.

https://doi.org/10.5194/wes-2026-9
Preprint. Discussion started: 10 February 2026

The assumption of completely eliminating all pitching moments in the aerodynamic model also has a minimal effect on the stability results. While it might be expected that this would lead to a large deviation, especially in the case of classical flap-twist mechanisms, the results for the edge-twist instability mechanism show relatively small differences. This highlights that the damping of the edgewise mode and the edge-twist flutter mechanism does differ significantly from the classical flap-twist mechanism.

The quasi-steady aerodynamic assumption, which neglects the unsteady lag effect introduced by the Theodorsen function, also results in little change in the stability analysis. This might initially seem counterintuitive, as the inclusion of unsteady effects is often critical in dynamic stability analyses. However, the relatively small reduced frequencies of the edgewise mode in this study make the quasi-steady assumption more valid, resulting in minimal impact on the stability characteristics.

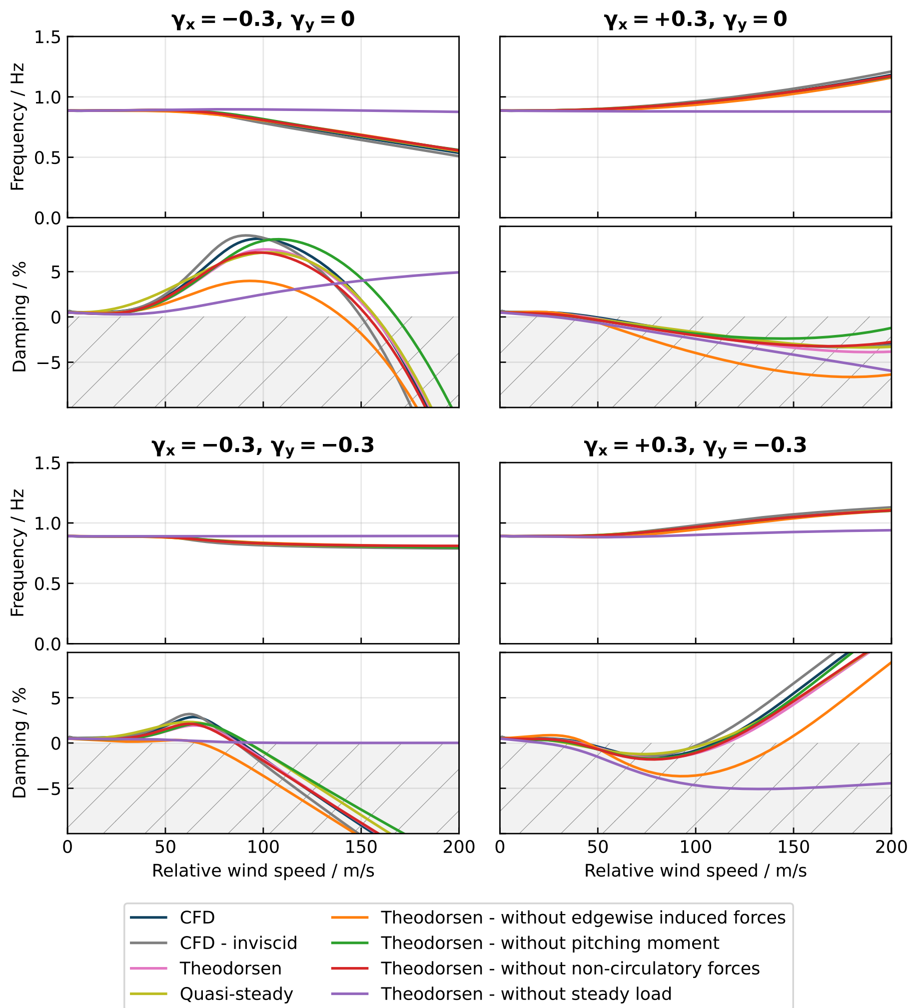

Figure 12. Sensitivity of the frequency and damping of the edgewise mode at a steady angle of attack of 7° for different modifications of the aerodynamic models. The model modifications are summarized in Table 3.

https://doi.org/10.5194/wes-2026-9
Preprint. Discussion started: 10 February 2026

Finally, neglecting non-circulatory forces has no significant effect on the stability results, which is consistent with expectations, as these forces generally contribute less to the overall stability in this context.

In summary, the comparison of stability results across the various aerodynamic model modifications reveals that some changes, such as the omission of the steady load and edgewise induced forces, have a pronounced effect on the stability analysis, while others, such as the inviscid assumption, the neglect of pitching moments, and the quasi-steady assumption, result in only minor changes. These findings suggest that certain aerodynamic effects, although seemingly secondary, can have a substantial impact on the stability and damping of the edgewise mode, while others that might be perceived as more significant have a relatively small influence. This also highlights that the sensitivities for the edge-twist flutter mechanism and the damping of the edgewise mode in general can differ drastically from those for a classical flap-twist flutter mechanism.

5 Flutter mechanism analysis

This section provides a deeper investigation of the fundamental flutter mechanism responsible for negative damping in edgewise modes. The aim is no longer to pursue the most precise quantitative solution, but rather to gain a qualitative understanding of the damping trends that were observed in section 3.

5.1 Approach to identify the fundamental instability mechanism

One of the most thorough, yet understandable explanations for the classical flap-twist flutter mechanism in subsonic flow was given by Bisplinghoff and Ashley (1962, §6-6). Bisplinghoff and Ashley analyzed the classical flap-twist mechanism on a highly simplified two-degree-of-freedom system, retaining only four quasi-steady aerodynamic terms. A similar approach is employed here. The full model is simplified to the greatest extent possible while preserving the qualitative trends in frequency, damping, and both the amplitude and phase of the mode shapes with respect to the relative wind speed. Importantly, the proposed simplification is intended exclusively to capture the damping of the edgewise mode and its instability mechanism; it is, for example, not a suitable simplification for investigating classical flap-twist flutter mechanisms.

To reduce the complexity of the structural model, the center of gravity offset relative to the elastic axis was removed, eliminating the off-diagonal terms in the mass matrix. Additionally, the structural damping was omitted. This significantly simplifies the equations of motion to

Reference: simplified structural model, full CFD aerodynamics

$$\begin{bmatrix} m & 0 & 0 \\ 0 & m & 0 \\ 0 & 0 & m\left(e_{cg}^2 + r^2\right) \end{bmatrix} \begin{Bmatrix} \ddot{x} \\ \ddot{y} \\ \ddot{\theta} \end{Bmatrix} + \begin{bmatrix} k_x & 0 & k_{x\theta} \\ 0 & k_y & k_{y\theta} \\ k_{x\theta} & k_{y\theta} & k_\theta \end{bmatrix} \begin{Bmatrix} x \\ y \\ \theta \end{Bmatrix} = \mathbf{f}_{\text{A,CFD}} \tag{41}$$

This model description with the full CFD aerodynamics will be used in this analysis as the reference result. Simplifying the aerodynamic model was a stepwise, trial-and-error process, progressively eliminating parameters. Figure 13 shows one of the

https://doi.org/10.5194/wes-2026-9
Preprint. Discussion started: 10 February 2026

eawe european academy of wind energy
Open Access WIND ENERGY SCIENCE DISCUSSIONS

steps in this process, where the sensitivity of each of the components in the aerodynamic $\boldsymbol{A}$ matrix is analyzed. Each transfer function in $\boldsymbol{A}$ is set to zero one at a time, and the resulting frequency and damping for the edgewise mode are shown relative to the CFD and Theodorsen reference results. It is apparent that, across all configurations, removing any of the three components F_{yy}, $F_{y\theta}$, or F_{xy} substantially changes the qualitative trend of the frequency and damping. Among the remaining components, F_{yx} and $F_{x\theta}$ have a quantitative significant impact, but do not change the overall trend. All other components have only a minor influence on the frequency and damping of the edgewise mode. This elimination process was continued by identifying the important terms within the F_{yy}, $F_{y\theta}$, and F_{xy} components. Finally, a quasi-steady aerodynamic model with only 3 terms remained. As a reminder, the complete set of low-fidelity terms of the full model is summarized in equations 31-40. The three remaining components are the edgewise force caused by the tilting of the steady load vector due to flapwise velocity, and the flapwise force induced by flapwise velocity and torsional deformation.

Simplified 3DOF model

$$\begin{bmatrix} m & 0 & 0 \\ 0 & m & 0 \\ 0 & 0 & m\left(e_{cg}^2+r^2\right) \end{bmatrix} \begin{Bmatrix} \ddot{x} \\ \ddot{y} \\ \ddot{\theta} \end{Bmatrix} + \begin{bmatrix} k_x & 0 & k_{x\theta} \\ 0 & k_y & k_{y\theta} \\ k_{x\theta} & k_{y\theta} & k_\theta \end{bmatrix} \begin{Bmatrix} x \\ y \\ \theta \end{Bmatrix} = \frac{1}{2}\rho W_0^2 2b C_{L_\alpha} \begin{Bmatrix} -\alpha_0 \frac{\dot{y}}{W_0} \\ -\frac{\dot{y}}{W_0} + \theta \\ 0 \end{Bmatrix} \tag{42}$$

Finally, one further simplification was introduced. The assumption is made that the kinematic relation between edgewise motion and torsional motion remains constant relative to the relative wind speed. This implies that the aerodynamic forces do not alter the edge-twist coupling. The fixed kinematic relation is defined as $x = B\theta$, with a constant coupling parameter B. Inserting this relationship into Eq. 42 allows the reduction of the three-degree-of-freedom system to a two-degree-of-freedom system. This results in

Simplified 2DOF model

$$\begin{bmatrix} m & 0 \\ 0 & mB \end{bmatrix} \begin{Bmatrix} \ddot{y} \\ \ddot{\theta} \end{Bmatrix} + \begin{bmatrix} k_y & 0 \\ 0 & k_x B \end{bmatrix} \begin{Bmatrix} y \\ \theta \end{Bmatrix} = \frac{1}{2}\rho W_0^2 2b C_{L_\alpha} \begin{Bmatrix} -\frac{\dot{y}}{W_0} + \theta \\ -\alpha_0 \frac{\dot{y}}{W_0} \end{Bmatrix}. \tag{43}$$

5.2 Flutter mechanism analysis results

This section explores the edge-twist instability mechanism and the trends in the damping of the edgewise mode by analyzing the underlying modal components of the edgewise mode. The analysis is conducted for the four cases that exhibit an unstable edgewise mode, focusing solely on the operating point with a steady angle of attack of 7°. The results obtained with the model shown in Eq. 41, which uses the full CFD aerodynamic forces, will serve as the reference result. The mechanisms are explained based on this reference. Note that similar results would be obtained if the aerodynamic forces of the Theodorsen based low-fidelity aerodynamic model or the corrected Stäblein model would have been used. Additionally, the stability analysis results obtained with the simplified 3 DOF model and simplified 2 DOF model are added to demonstrate that these models, despite their simplicity, capture the main trends in the edgewise mode's damping behavior.

https://doi.org/10.5194/wes-2026-9
Preprint. Discussion started: 10 February 2026

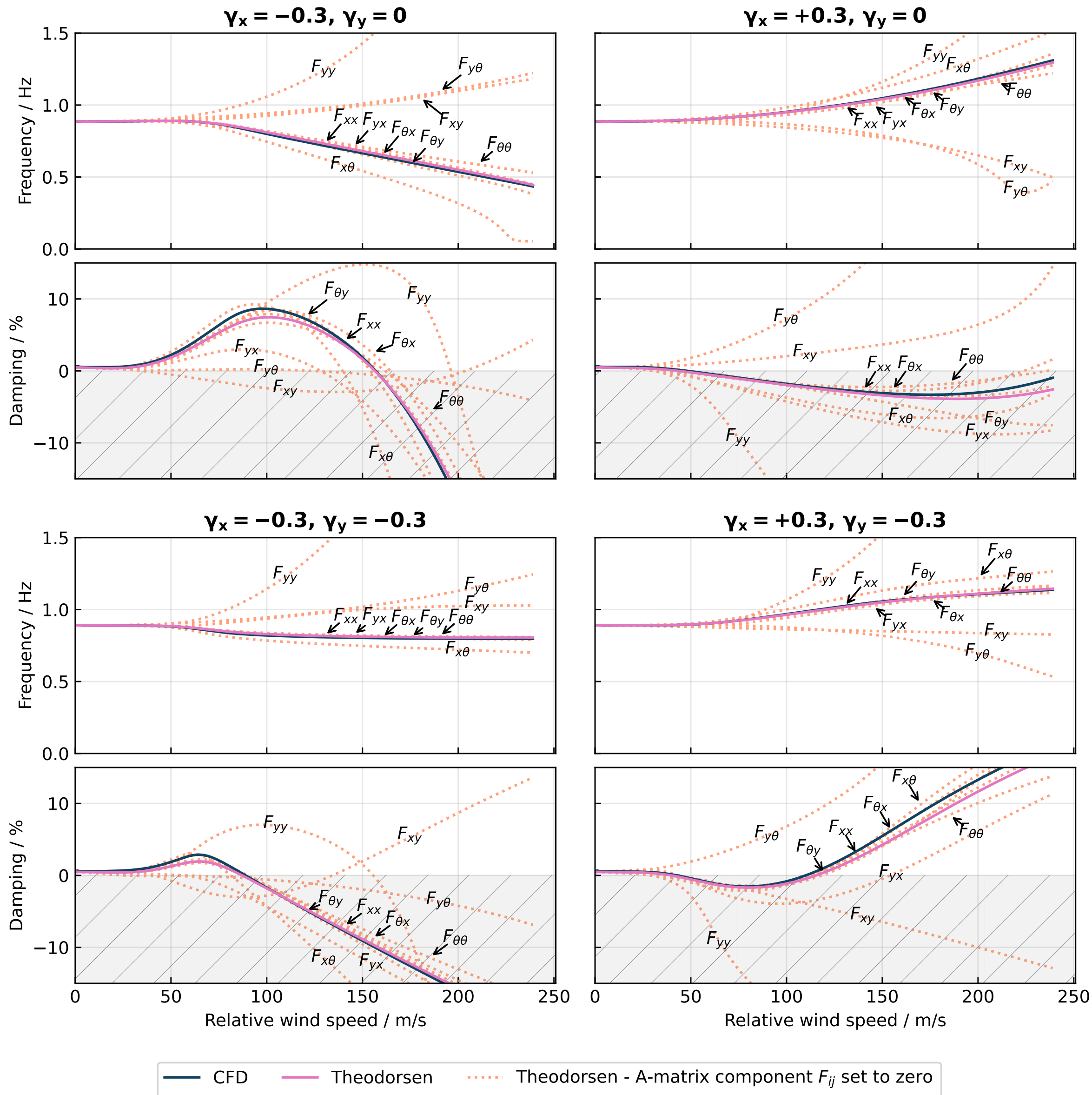

Figure 13. Sensitivity of the edgewise branch on each individual transfer function of the aerodynamic **A** matrix. Each dotted line shows the edgewise branch for a new stability analysis with Theodorsen forces, but the labeled component omitted (set to zero).

Edge-twist coupling to feather ($\gamma_x = -0.3$), no flap-twist coupling ($\gamma_y = 0$)

Figure 14 shows the flutter mechanism analysis for the case with edge-twist coupling to feather ($\gamma_x = -0.3$) and without flap-twist coupling ($\gamma_x = 0$). This figure shows the key modal components essential for understanding the damping trend of the edgewise mode. This figure contains a lot of information in the various subplots. So, for this first case, the results in each of the subplots and the connections between the results in the different subplots will be explained in detail. The results for the CFD reference model are shown in dark blue, the results for the simplified models are shown in green and pink. Initially, the discussion centers on the dark blue reference results to establish a clear understanding of the trends observed in each subplot. After fully explaining the behavior of the reference model, comparisons with the two simplified models are made. The line styles are used to differentiate between the different degrees of freedom. In all subplots, the solid line corresponds to the edgewise degree of freedom, the dashed lines implies the flapwise degree of freedom and the dotted line indicates the torsional degree of freedom. While the specific quantities vary between the plots (e.g. displacement, force, force induced by a specific degree of freedom), the line styles consistently follow this convention.

Figures 14(a) and 14(b) show the frequency and damping of the edgewise mode, while figures 14(d) and 14(e) illustrate the displacement modal components in terms of amplitude and phase, both referenced to torsion. In figure 14(d), the solid line represents the edgewise displacement amplitude relative to torsion, while the dashed line represents the flapwise displacement relative to torsion. At a relative wind speed of $0\,\mathrm{m\,s^{-1}}$, these ratios are entirely governed by structural coupling, indicating that there is no flapwise displacement in the edgewise mode at zero wind speed. As the relative wind speed increases, the flapwise displacement amplitude increases rapidly, while the edgewise displacement remains relatively constant, unaffected by aerodynamic forces. Around $100\,\mathrm{m\,s^{-1}}$, the flapwise displacement amplitude surpasses the edgewise displacement, suggesting that at higher wind speeds, the edgewise mode exhibits a greater displacement amplitude perpendicular to the chord than parallel to it. Figure 14(e) shows the phase relationship between the flapwise and edgewise displacements relative to torsion. A positive phase angle implies that flapwise or edgewise displacement leads torsion, while a negative phase angle implies that flapwise or edgewise displacement trails torsion. The phase of the edgewise displacement remains nearly constant, with little variation as aerodynamic forces increase. In contrast, the phase of the flapwise displacement shifts significantly, moving from $-360°$ (out-of-phase with torsion) to $-180°$ (trailing torsion), gradually becoming more in-phase with torsion as the relative wind speed increases, with torsion always leading the flapwise displacement.

Figures 14(f) and 14(g) illustrate the amplitude of the forces in each direction per degree of torsion, as well as the phase between these forces and the modal velocities in the respective directions. The amplitudes of both torsional and edgewise forces steadily increase with wind speed. Initially, the amplitude of the flapwise force increases but eventually decreases to zero at around $160\,\mathrm{m\,s^{-1}}$. The phase relationship between force and velocity indicates whether each force component is stabilizing or destabilizing. Forces are stabilizing when out-of-phase with velocity (green region) and destabilizing when in-phase (red region). The torsional force is destabilizing over most of the wind speed range, while the edgewise force stabilizes at lower speeds but becomes destabilizing at higher wind speeds. Finally, the flapwise force is stabilizing at lower wind speeds but becomes destabilizing due to a $180°$ phase shift at approximately $160\,\mathrm{m\,s^{-1}}$.

The relative importance of the stabilizing or destabilizing effect in each direction depends on both the phase and amplitude of the forces. This can be assessed by computing the aerodynamic work as the product of the modal force and velocity in each direction. Figure 14(c) shows the computed aerodynamic work in each direction, along with the combined total aerodynamic work. The agreement with the damping diagram verifies the analysis. Without structural damping, the damping of the system

https://doi.org/10.5194/wes-2026-9
Preprint. Discussion started: 10 February 2026

becomes negative when the performed aerodynamic work becomes positive. This figure mainly reveals that it is particularly the aerodynamic work performed in flapwise direction which contributes most to the total aerodynamic work. Therefore, to further investigate the flapwise force component, figures 14(h) and 14(i) show the amplitude and phase of the flapwise force induced by motion in each individual degree of freedom. The solid, dashed and dotted lines therefore imply the flapwise force components induced by edgewise, flapwise and torsional motion, respectively. The amplitude of the flapwise force induced by edgewise motion is minimal, while the forces induced by torsional and flapwise motion are comparable in magnitude. The torsion-induced force is initially slightly smaller but becomes larger than the flap-induced force at wind speeds above $160\,\mathrm{m\,s^{-1}}$. Figure 14(i) shows the phase of the flapwise force components relative to flapwise velocity. The phase of the force induced by flapwise motion remains nearly $180°$ out-of-phase with the flapwise velocity. However, the phase between the flapwise force induced by torsional motion and the flapwise velocity decreases with increasing wind speed, shifting from stabilizing (out-of-phase) to destabilizing (in-phase).

Altogether, these diagrams illustrate a straightforward mechanism. The aerodynamic work decomposition in subplot (c) shows that the total aerodynamic work is dominated by the work in flapwise direction. The decomposition of the flapwise force in subplot (h) shows that the total flapwise force has two main components; the flapwise force induced by flapwise motion and by torsional motion. The flapwise force induced by flapwise motion is stabilizing due to the approximately constant phase of $180°$ relative to the flapwise velocity (subplot (i)). The effect of the flapwise force induced by torsional motion depends on the phase angle between flapwise motion and torsional motion (subplot (e)). The phase between flapwise motion and torsional motion shifts from out-of-phase towards torsion leading flapwise displacement. This causes the phase between the flapwise force induced by torsional motion and flapwise velocity to shift from out-of-phase to fully in-phase at approximately $150\,\mathrm{m\,s^{-1}}$ (subplot (i)). The total aerodynamic work and damping of the system then depends on the relative amplitude and phase of these two components. At lower relative wind speeds, the amplitude of the flapwise force induced by flapwise motion is slightly higher than the amplitude of the flapwise force induced by torsional motion, but at higher wind speed this switches, causing the destabilizing effect of the flapwise force due to torsion to prevail, leading to the instability of the edgewise mode.

Now, focusing attention onto both simplified models and comparing their results with the CFD reference result, it is clear that the fundamentally critical trends discovered for the stability analysis with the CFD aerodynamics are also present for the simplified models. The trends in the flapwise-torsional phase are similar, with exception of the phase at low wind speeds. Correspondingly, the trends in both the amplitude and the phase of the flapwise forces induced by flapwise motion and torsional motion are similar to the reference result, leading to similar trends in the aerodynamic work and damping. The ground for the good agreement of the simplified 2 DOF model can be seen in the amplitude and phase of the edgewise component of the CFD reference result shown in figures 14(d) and 14(e). Both the amplitude and the phase of the edgewise displacement relative to torsion are nearly constant with respect to relative wind speed, justifying the assumption of a fixed kinematic relationship between both degrees of freedom, which was used to eliminate one degree of freedom from the system.

https://doi.org/10.5194/wes-2026-9
Preprint. Discussion started: 10 February 2026

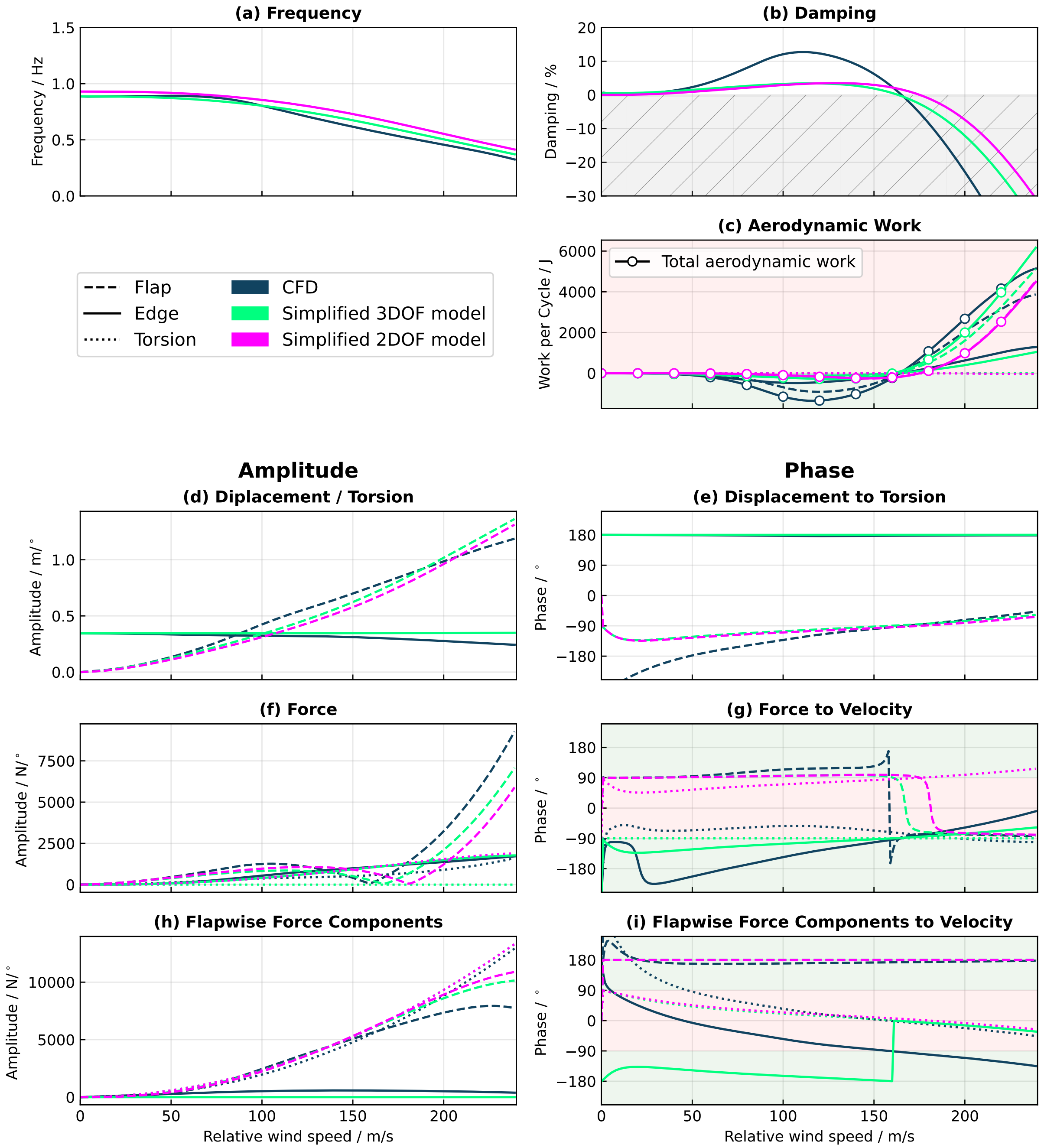

Figure 14. Flutter mechanism analysis of the edgewise mode for $\gamma_x = -0.3$, $\gamma_y = 0$, AOA$= 7^\circ$. (a) frequency, (b) damping, (c) aerodynamic work in each direction and in total, (d) displacement amplitude in flapwise and edgewise direction normalized by torsion, (e) phase between the flapwise and edgewise modal displacements and the torsional modal displacement, (f) force amplitude in each direction per degree of modal torsion, (g) phase between force in each direction and modal velocity in the same direction, (h) amplitude of the flapwise force components induced by each of the degrees of freedom, (i) phase between the flapwise force components and the flapwise velocity

https://doi.org/10.5194/wes-2026-9
Preprint. Discussion started: 10 February 2026

Edge-twist coupling to stall ($\gamma_x = 0.3$), no flap-twist coupling ($\gamma_y = 0$)

Figure 15 shows the flutter mechanism analysis for the system configuration with edge-twist coupling to stall. Explaining the mechanism for this case can be done by following the same reasoning as for the case with edge-twist coupling to feather. Again, the total aerodynamic work remains predominantly influenced by the work in the flapwise direction. And as in the previous case, this work is mainly the result of the combination between the flapwise force due to flapwise motion and the flapwise force induced by torsional motion. Therefore, the aeroelastic stability is governed by the relative amplitude differences and the phase angles of these two components. In contrast to the previous case, the flap-torsion phase relationship as a function of relative wind speed in subplot (e) exhibits a different trend. It remains nearly constant, with torsion lagging by slightly over $90°$. This results in a nearly constant in-phase oscillation between the flapwise force induced by torsion and the flapwise velocity, as shown in subplot (i). Additionally, comparing subplot (d) between figure 15 and 14 shows that the flapwise amplitude is relatively smaller than in the case with edge-twist coupling to feather. Consequently, the amplitude of the flapwise force induced by torsion is greater than the flapwise force induced by flapwise motion (subplot (h)). This combination of a smaller stabilizing flapwise force (due to flapwise motion) and a larger destabilizing flapwise force (induced by torsional motion) leads to positive aerodynamic work across nearly all wind speeds. This, in turn, results in a negative damping of the edgewise mode for nearly the entire range of relative wind speeds.

Note that an instability at near-zero wind speeds is in practice not realistic. This is a result of the elimination of the structural damping and coupling in the mass matrix used in this chapter. Nevertheless, the behavior of this simplified model is still a good approximation of the full model, which shows a very low damping of the edgewise mode and low flutter point for this case with edge-twist coupling to stall and no flap-twist coupling, as could already be seen in figure 9.

Similar to the previous case, the simplified 3DOF model and the simplified 2DOF model successfully capture the trends in all relevant modal properties.

https://doi.org/10.5194/wes-2026-9
Preprint. Discussion started: 10 February 2026

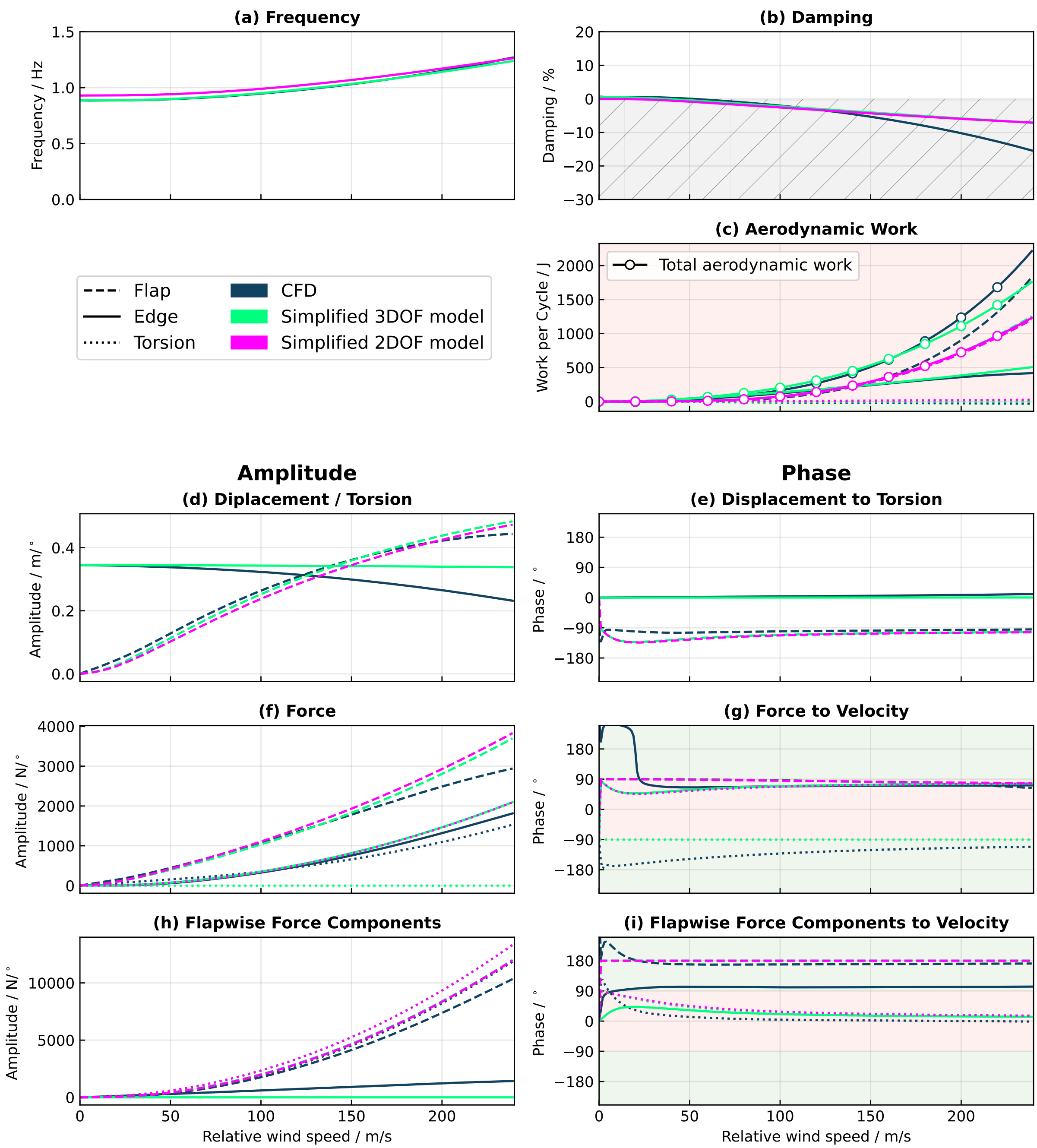

Figure 15. Flutter mechanism analysis / $\gamma_x = +0.3$, $\gamma_y = 0$, AOA$= 7^\circ$. (a) frequency, (b) damping, (c) aerodynamic work in each direction and in total, (d) displacement amplitude in flapwise and edgewise direction normalized by torsion, (e) phase between the flapwise and edgewise modal displacements and the torsional modal displacement, (f) force amplitude in each direction per degree of modal torsion, (g) phase between force in each direction and modal velocity in the same direction, (h) amplitude of the flapwise force components induced by each of the degrees of freedom, (i) phase between the flapwise force components and the flapwise velocity

https://doi.org/10.5194/wes-2026-9
Preprint. Discussion started: 10 February 2026

Edge-twist coupling to feather ($\gamma_x = -0.3$), flap-twist coupling to feather ($\gamma_y = -0.3$)

Figure 16 shows the flutter mechanism analysis for the system configuration with both edge-twist coupling to feather and flap-twist coupling to feather. Introducing structural flap-twist coupling significantly alters the amplitude and phase of both the edgewise component and flapwise component in comparison to the case without structural flap-twist coupling. Both the amplitude and phase relationship between edgewise and torsional motion, shown in subplots (d) and (e), are no longer constant with respect to the relative wind speed. The amplitude of the flapwise component is relatively smaller compared to the case without structural flap-twist coupling. This causes the amplitude of the flapwise force induced by flapwise motion to be smaller than the amplitude of the flapwise force induced by torsional motion (subplot (h)). The stabilizing effect of the flapwise induced force is therefore smaller compared to the case without flap-twist coupling, leading to a smaller increase in damping up to approximately $70\,\mathrm{m\,s^{-1}}$, and an earlier flutter point at approximately $90\,\mathrm{m\,s^{-1}}$, compared to approximately $160\,\mathrm{m\,s^{-1}}$ for the case without flap-twist coupling.

The simplified 3DOF model is still a good approximation of the full CFD reference result. However, the relationship between edgewise and torsional motion is no longer constant, which makes the assumption used for the simplified 2-DOF model invalid. As a result, the simplified 2-DOF model does not match well with the CFD or simplified 3-DOF model results, highlighting a limitation of this simplified model when flap-twist coupling is present.

Edge-twist coupling to feather ($\gamma_x = -0.3$), flap-twist coupling to feather ($\gamma_y = -0.3$)

Figure 17 shows the flutter mechanism analysis for the system configuration with edge-twist coupling to stall and flap-twist coupling to feather. This configuration can be compared with Figure 15, which shows the same edge-twist coupling to stall without flap-twist coupling. The initial trend in all modal parameters is the same, resulting in the same immediate increase in aerodynamic work and reduction in damping. However, in contrast to the case without structural coupling, the flapwise amplitude is relatively higher and increases further at higher wind speeds. This results in a larger stabilizing flapwise force and an increase in damping starting at approximately $90\,\mathrm{m\,s^{-1}}$ wind speed.

The simplified 2DOF model captures the mechanism which leads to the initial reduction in damping, but it fails to capture the subsequent increase in damping at higher wind speeds. The trends of the modal components computed with the simplified 3DOF model match well with the CFD reference result.

https://doi.org/10.5194/wes-2026-9
Preprint. Discussion started: 10 February 2026

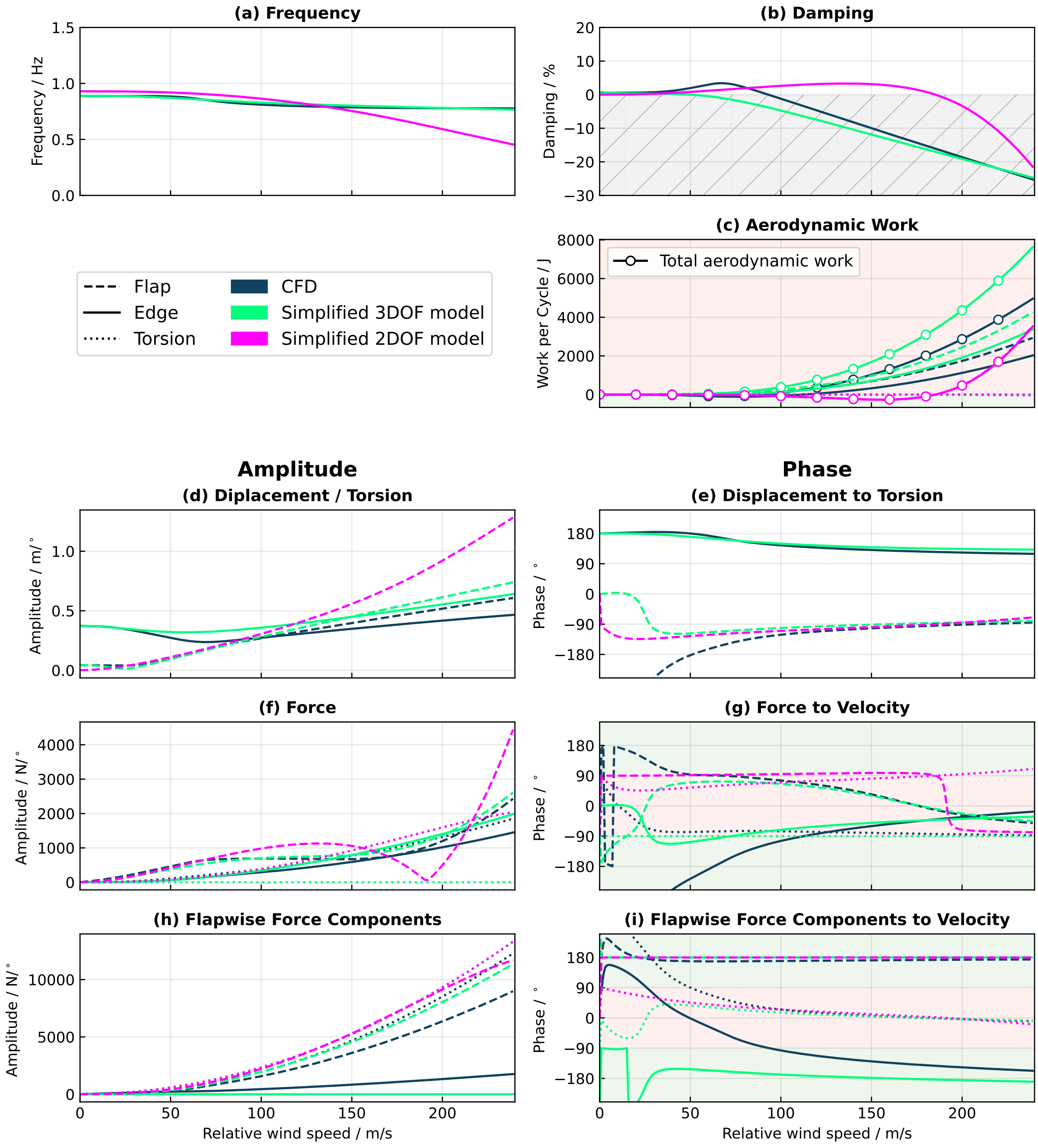

Figure 16. Flutter mechanism analysis / $\gamma_x = -0.3$, $\gamma_y = -0.3$, AOA$= 7^{\circ}$. (a) frequency, (b) damping, (c) aerodynamic work in each direction and in total, (d) displacement amplitude in flapwise and edgewise direction normalized by torsion, (e) phase between the flapwise and edgewise modal displacements and the torsional modal displacement, (f) force amplitude in each direction per degree of modal torsion, (g) phase between force in each direction and modal velocity in the same direction, (h) amplitude of the flapwise force components induced by each of the degrees of freedom, (i) phase between the flapwise force components and the flapwise velocity

https://doi.org/10.5194/wes-2026-9
Preprint. Discussion started: 10 February 2026

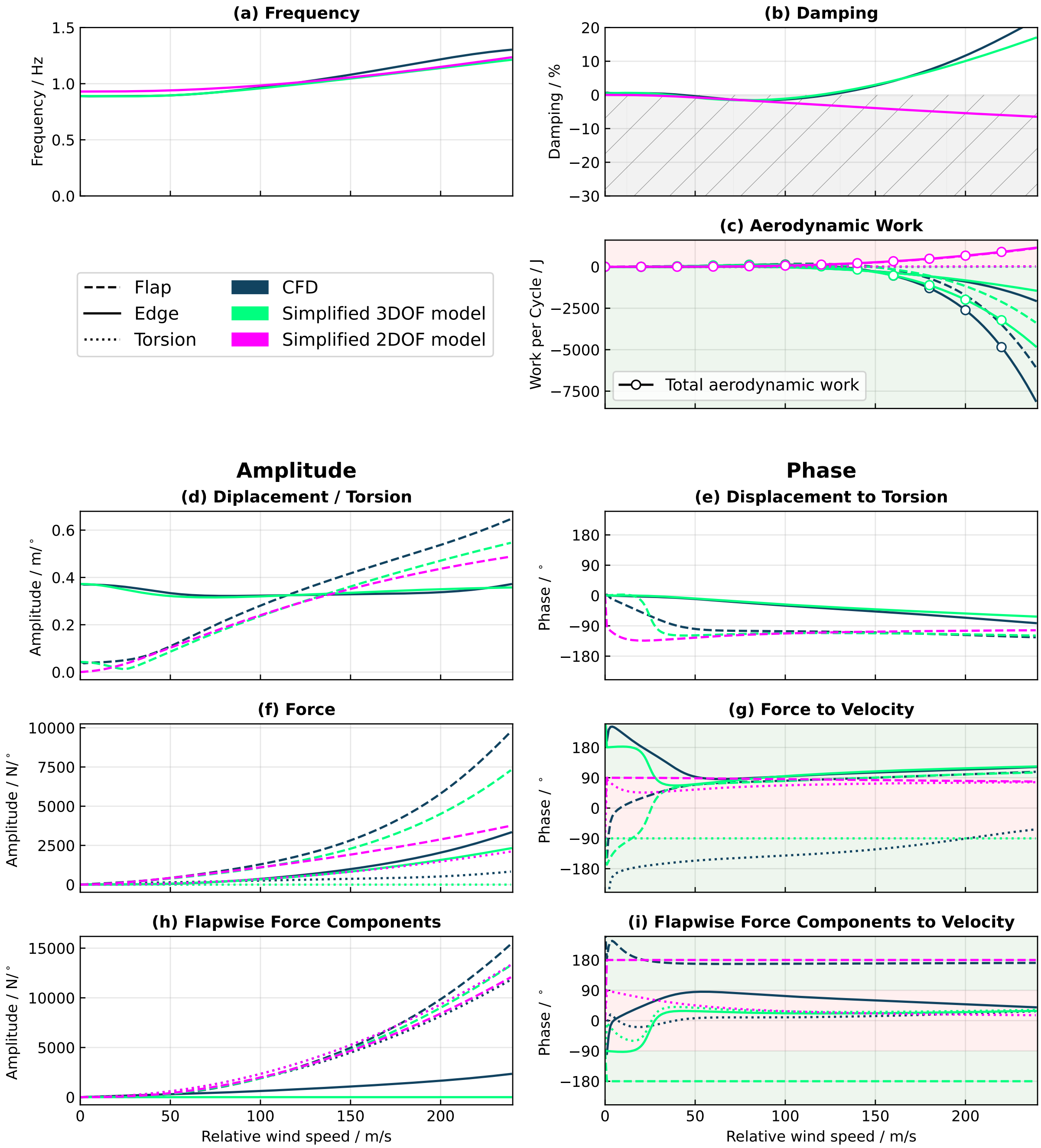

Figure 17. Flutter mechanism analysis / $\gamma_x = 0.3$, $\gamma_y = -0.3$, AOA$= 7°$. (a) frequency, (b) damping, (c) aerodynamic work in each direction and in total, (d) displacement amplitude in flapwise and edgewise direction normalized by torsion, (e) phase between the flapwise and edgewise modal displacements and the torsional modal displacement, (f) force amplitude in each direction per degree of modal torsion, (g) phase between force in each direction and modal velocity in the same direction, (h) amplitude of the flapwise force components induced by each of the degrees of freedom, (i) phase between the flapwise force components and the flapwise velocity

https://doi.org/10.5194/wes-2026-9
Preprint. Discussion started: 10 February 2026

Summary of the instability mechanism analysis

The analysis of the flutter mechanisms across all four cases leads to several key insights. In all scenarios, the damping of the edgewise mode is primarily influenced by the flap-torsional modal components, along with their relative amplitudes and phase relationships. This interaction is only possible because of the structural edge-twist coupling, which allows edgewise forces to affect torsional motion, thereby inducing an additional aerodynamic flap-twist coupling. Consequently, the term "edge-twist flutter" may be somewhat misleading. The coupling responsible for positive work is not an aerodynamic edge-twist coupling per se, but rather the interaction between the flapwise and torsional forces and motions within the edgewise mode. In this regard, the mechanism closely resembles classical flap-twist flutter, although the responsible aerodynamic coupling terms are vastly different. This distinction is demonstrated by the simplified 3DOF model, which includes only three quasi-steady aerodynamic terms that contrast with those required to explain a classical flap-twist flutter mechanism (Bisplinghoff and Ashley, 1962). For simpler cases without structural flap-twist coupling, the 2DOF model underlines that the edge-twist flutter mechanism is essentially a two-degree-of-freedom flutter problem.

The explanation given here is more elaborate, but does not differ significantly from the one given in Stäblein et al. (2017a, b) in its essence. In the authors' opinion, both this current analysis on the underlying driving mechanism, as well as other studies, to the best of their knowledge, remain inconclusive. While it provides a detailed breakdown of the modal components that lead to positive aerodynamic work and negative damping, it does not adequately explain why the trends observed in these components with respect to the relative wind speed occur. For instance, it does not clarify why the flap-torsional phase angle evolves in a particular manner, nor why the flapwise amplitude varies between cases. Furthermore, the analysis does not fully link the force components to changes in modal behavior as a function of the relative wind speed. This is a challenging task for fully coupled models. Future research should aim to address these gaps, potentially following approaches similar to those proposed by Patel and Lefas (2025) or Bisplinghoff and Ashley (1962, §6-6).

6 Conclusions

This study aimed to assess the accuracy of low-fidelity aerodynamic models in predicting the damping of edgewise modes and to investigate the fundamental mechanisms driving edgewise instabilities in wind turbine blades. A two-dimensional, three-degree-of-freedom model, based on parameters representative of the DTU 10 MW rotor blade design, was used for the analysis. The results of the stability analysis were compared among three models: a high-fidelity computational fluid dynamics (CFD) reference model, a low-fidelity aerodynamic model, and a low-fidelity literature reference.

The direct comparison of the frequency domain aerodynamic forces between the high-fidelity and low-fidelity approaches reveals a good agreement for most components, but a poor agreement for some of the aerodynamic force components induced by edgewise motion. Despite these discrepancies, only small differences exist in the stability results between the high-fidelity CFD model and the low-fidelity Theodorsen-based approach. After correcting the literature reference, the results from this model were found to align well with the CFD reference. All trends are captured well, and the flutter points, as well as the damping of the edgewise mode showed strong agreement across all models.

https://doi.org/10.5194/wes-2026-9
Preprint. Discussion started: 10 February 2026

A sensitivity study on the influence of specific aerodynamic terms demonstrated a significant dependence on steady load, and a smaller, but still quantitatively relevant, dependence on forces induced by edgewise motion. In contrast, unsteady aerodynamic effects, pitching moments, viscous effects, and non-circulatory force components had minimal impact on the damping of the edgewise mode.

The flutter mechanism was analyzed through analysis of the modal components, forces, and aerodynamic work. The present analysis agrees with the findings in Stäblein et al. (2017a, b) and showed that the edgewise flutter mechanism is primarily driven by the phase difference between flapwise and torsional motion within the edgewise mode. The torsional motion, which is enabled by structural edge-twist coupling, is critical in this mechanism. Notably, the relevant coupling is not a direct flapwise-torsional coupling, but rather a coupling between the structurally coupled edge-torsional motion and flapwise motion. This finding suggests that the aerodynamic coupling terms required for edgewise flutter differ from those of the classical flap-twist flutter mechanism. This was demonstrated by a comparison of the flutter mechanism with an aerodynamic model with only three quasi-steady aerodynamic terms, which agreed qualitatively well with the full results obtained with the full CFD aerodynamic model. Further simplification of the system to a two-degree-of-freedom model highlighted the fundamental coupling between flapwise motion and the structurally coupled edge-torsional motion. Finally, the trends in the edgewise damping can in most cases be understood by an analysis of the amplitude and phase of the destabilizing flapwise force induced by torsional motion and the stabilizing flapwise force induced by flapwise motion.

The study found that both edge-twist coupling to feather and edge-twist coupling to stall will lead to an edgewise instability. Specifically, for edge-twist coupling to stall, the critical inflow speed decreases with increasing steady load, whereas for edge-twist coupling to feather, the critical inflow speed increases with steady load. If, in addition to edge-twist coupling, flap-twist coupling to feather is present, the critical relative inflow speed is further reduced.

The presented analysis is based on three main assumptions and limitations. First, the study is limited to a two-dimensional, three-degree-of-freedom model. Second, the model parameters are derived from a single blade design. Third, the study focuses on an operating point in attached flow conditions. The validity of using such a simplified model to represent the complex dynamics of a full turbine requires further verification. Stäblein et al. (2017a) demonstrated similar trends and sensitivities in full blade and turbine analyses but did not directly compare results between a full turbine model and a reduced-order model. To enable better generalization of these findings, it would be beneficial to assess the sensitivities of the results to model parameters from other blade designs, such as those with different blade frequencies or aerodynamic properties. Future work should also focus on extending the current analysis to other operating conditions, including detached flow, where the discrepancies between high- and low-fidelity models are expected to be more pronounced.

Several open questions and potential areas for future research remain. For instance, while the presented discussion of the flutter mechanism is thorough, it remains descriptive rather than explanatory. Further investigations are needed to fully understand the underlying causes of the flutter mechanism. Furthermore, the simplified model could be validated through wind tunnel experiments, and validation efforts on real wind turbines should continue to ensure the robustness of the findings.

https://doi.org/10.5194/wes-2026-9
Preprint. Discussion started: 10 February 2026

Code availability. The updated state-space model for the Stäblein methodology is available on Github: https://github.com/DLR-AE/jfs_
795 2016. The other aerodynamic methodologies as well as the flutter analysis code can not be shared at this time.

Appendix A: Difference between a fixed or moving frame of reference

A typical section, as studied in this work, can represent different physical systems. The most common application is for it to represent an elastic structure, such as an aircraft wing or wind turbine rotor blade. In this case the degrees of freedom of the typical section, in this study the edgewise motion, flapwise motion and torsional motion, represent the generalized degrees
800 of freedom of the elastic structure, e.g. an edgewise mode, a flapwise mode and a torsional mode. The structural dynamic properties of the typical section are defined in a way to represent the properties of the generalized degrees of freedom of the elastic structure. The typical section could, however, also be used to represent the flight mechanics of a free-flying object. The degrees of freedom of the typical section then represent the translational and rotational degrees of freedom of the whole object. The distinction between these two options lies in the definition of a fixed versus a moving reference system. Figure A1 offers
805 simplified illustrations that help clarify this subtle difference. The properties of the degrees of freedom of an elastic system are defined in a fixed reference system. For example, edgewise stiffness is defined along the fixed x direction, regardless of the elastic $d\theta$ at a certain point along the blade. To illustrate, consider a blade with a highly flexible outer section. Even if the elastic torsional deformation of an outboard section is 90° and the profile tip points in y direction, the edgewise mode, defined by the edgewise stiffness and edgewise frequency, will still move in the global x direction. In contrast, the flight-mechanical
810 properties of an aircraft are defined relative to a moving frame that follows the aircraft's orientation.

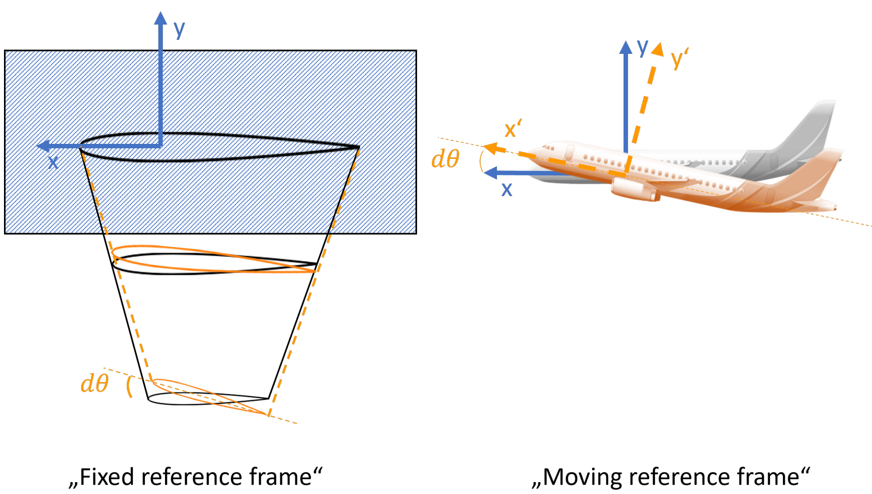

Figure A1. Physical interpretation for the definition of a fixed or moving reference frame

The definition of the reference system does not depend on the aerodynamic methodology. The high-fidelity CFD aerodynamic model as well as the low-fidelity model can be used with either of these definitions. Figure A2 shows the frequency

https://doi.org/10.5194/wes-2026-9
Preprint. Discussion started: 10 February 2026

domain aerodynamic forces for the CFD and Theodorsen methodologies used in this paper, which applied the fixed reference system, in comparison with the CFD and Theodorsen forces using the moving reference system. The main effect of the fixed vs. moving reference system is an offset in the real part of the $F_{x\theta}$ component, the force in edgewise direction induced by torsional motion. The offset is the same in the high-fidelity and low-fidelity method. In all other components the definition of the reference system does not significantly affect the result.

The ground for the offset can be understood by looking into the quasi-steady derivation of $F_{x\theta} = \frac{dF_x}{d\theta}$, visualized in figure A3. Assume the blade section subjected to a steady angle of attack α_0, resulting in the steady lift L_0. Using first the fixed reference system definition, $F_{x\theta}$ can be computed by taking the finite difference with an infinitesimal $d\theta$.

$$F_{x\theta} = \frac{dF_x}{d\theta} = \frac{F_{x_1} - F_{x_0}}{\theta_1 - \theta_0} \tag{A1}$$

The infinitesimal increase in pitch angle $d\theta$ will cause an infinitesimal increase in lift by $dL = C_{L_\alpha} d\theta$. F_{x_0} and F_{x_1} can be computed by the projection of the lift force in x direction. Inserting this in A1 and using a small angle approximation results in

$$F_{x\theta} = \frac{(L_0 + dL)\sin(\alpha_0) - L_0 \sin(\alpha_0)}{d\theta} = \frac{C_{L_\alpha} d\theta \alpha_0}{d\theta} = C_{L_\alpha}\alpha_0. \tag{A2}$$

Now, if instead of a fixed reference system, the reference system would rotate with the body, illustrated as the $x' - y'$ reference system in figure A3, the steady derivative $F_{x'\theta}$ can be computed in an analogous manner, this time projecting the total lift force into the x' direction. This leads to

$$F_{x'\theta} = \frac{(L_0 + dL)\sin(\alpha_0 + d\theta) - L_0 \sin(\alpha_0)}{d\theta} = \frac{\cancel{L_0\alpha_0} + L_0 d\theta + dL\alpha_0 + \cancel{dLd\theta} - \cancel{L_0\alpha_0}}{d\theta} = \frac{L_0 d\theta + C_{L_\alpha} d\theta \alpha_0}{d\theta} = L_0 + C_{L_\alpha}\alpha_0, \tag{A3}$$

where the $dLd\theta$ term is canceled because it is a product of two infinitesimal terms. Comparing the final expression for $F_{x\theta}$ in Eq. A2 and for $F_{x'\theta}$ in Eq. A3 shows the difference of L_0, which matches with the offset seen in figure A2, solely caused by the definition of a fixed or moving reference system.

More intuitively, this difference can also be seen in figure A3. The difference between the two reference systems is an infinitesimal variation $d\theta$ in pitch. However, because the steady lift vector L_0 is not infinitesimal, the projection of this steady lift vector in either x or x' direction causes a difference. This also illustrates that the difference between both definitions diminishes with a smaller steady lift force and disappears if the section has no steady lift.

https://doi.org/10.5194/wes-2026-9
Preprint. Discussion started: 10 February 2026

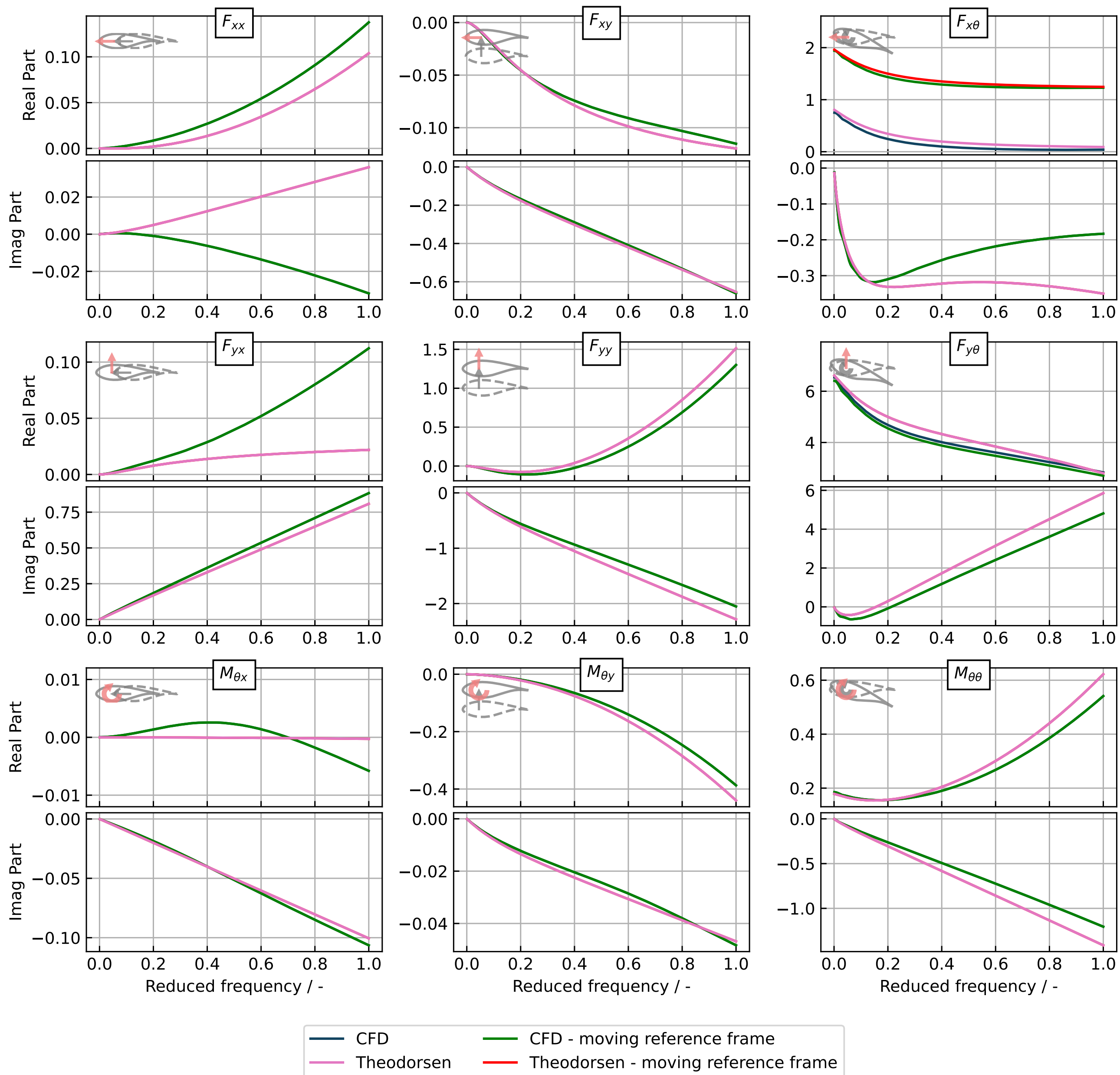

Figure A2. Comparison of the frequency domain transfer functions of the aerodynamic A matrix from Eq. 6 determined by the high-fidelity CFD approach with a fixed reference frame, the low-fidelity Theodorsen based approach with a fixed reference frame, the high-fidelity CFD approach with a moving reference frame, and the low-fidelity Theodorsen based approach with a moving reference frame

https://doi.org/10.5194/wes-2026-9
Preprint. Discussion started: 10 February 2026

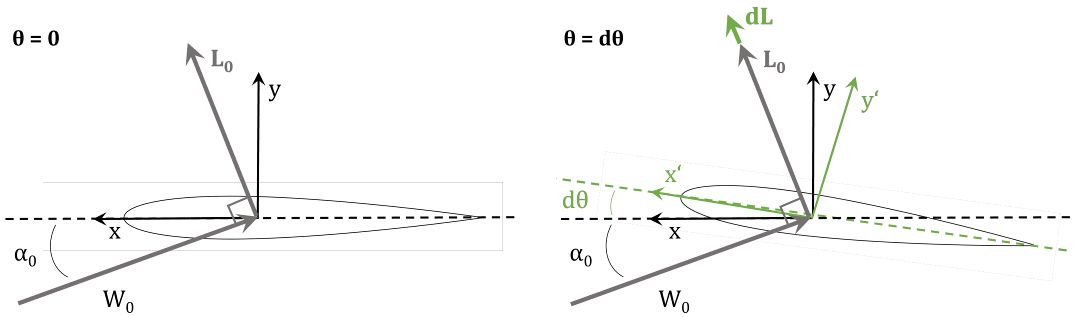

Figure A3. Supporting figure for the derivation of the steady component $\frac{dF_x}{d\theta}$

Finally, the influence of reference frame definition is illustrated in figure A4, showing the flutter analysis results for the six selected cases, also discussed in section 3.3. Results are shown for the CFD and Theodorsen implementation using the fixed reference frame, as used in the paper, and for the CFD and Theodorsen implementation using the moving reference frame. The influence reference frame definition on the flap and torsional mode and on the classical flap-twist flutter mechanism is minimal, which are therefore blended out in the background. The influence of the definition on the edgewise mode is in all cases severe for higher wind speeds. For the cases with edge-twist coupling to feather ($\gamma_x = -0.3$), the initial increase in damping is similar for both definitions, but the strong decrease in damping for the models with the fixed reference frame is not present in the models applying the moving reference frame. For the cases with edge-twist coupling to feather ($\gamma_x = +0.3$), the reduction in damping and corresponding instability is similar for both definitions, but the increase in damping at higher wind speeds is not, or less prominent, in the models with the moving reference frame. Also in the modal frequencies the significant frequency decrease for the edge-twist to feather coupled system and the frequency increase for the edge-twist to stall coupled system are not present in the models with the moving reference frame.

In summary, the comparisons in this appendix show that a seemingly small difference in the definition of the reference systems can result in a large discrepancy in the stability analysis of the edgewise mode, because of its strong dependency on the influence of the steady load vector on the edgewise force induced by torsional motion, which is important for an accurate modeling of the damping of the edgewise mode.

https://doi.org/10.5194/wes-2026-9
Preprint. Discussion started: 10 February 2026

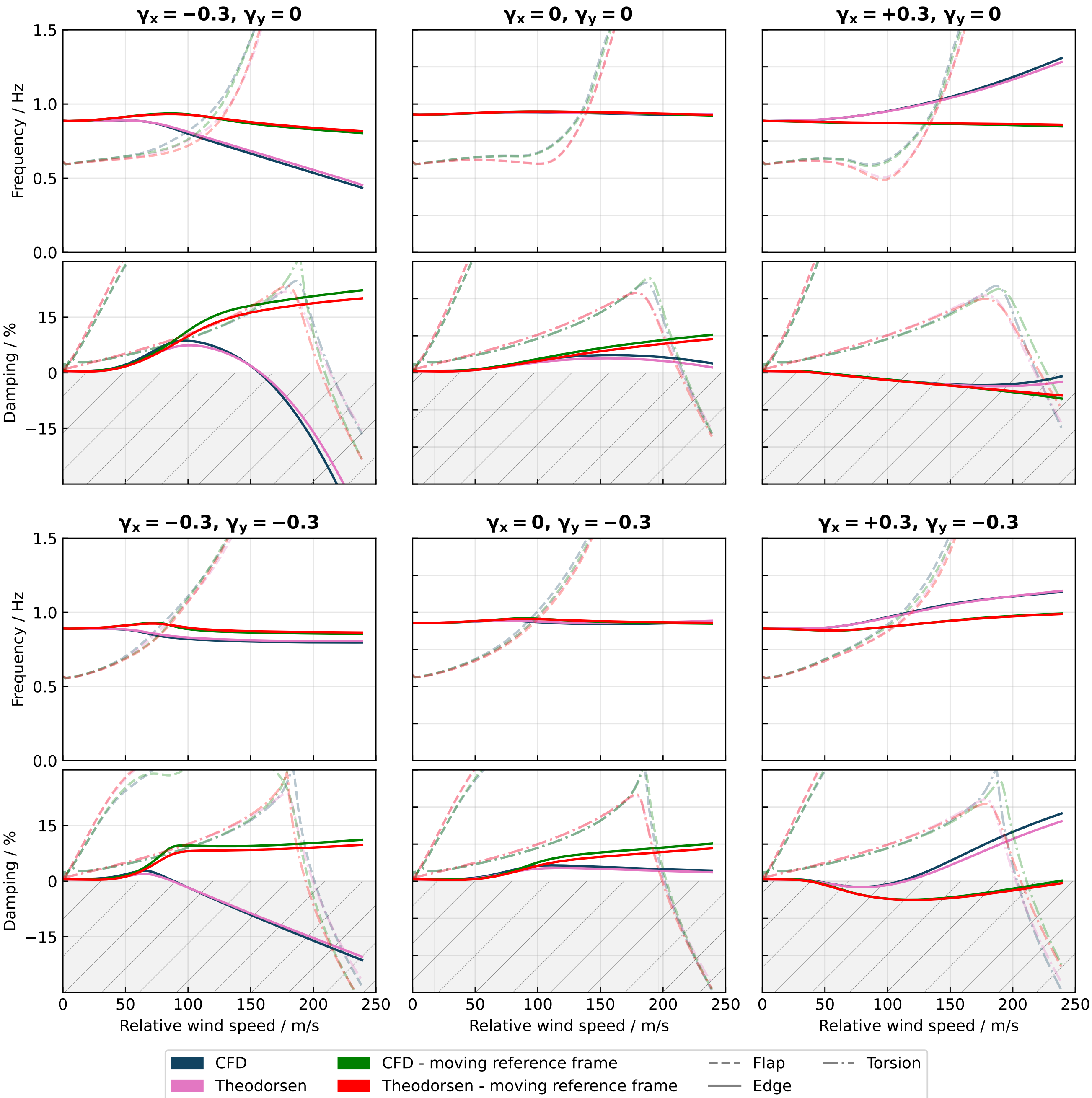

Figure A4. Frequency and damping of the edgewise mode for the six selected cases at a steady angle of attack of 7°. Comparison between the CFD and Theodorsen results based on the fixed and moving frame of reference.

Author contributions. HV was the principal researcher for this work responsible for the literature study, conceptualization, implementation of the methods, analysis of the results, and writing of the paper. OH provided support and advice throughout all steps, including extensive reviewing and improving of the final paper.

Competing interests. The authors have no competing interests to declare.

Acknowledgements. This work builds upon previous research of Alexander Stäblein, Morten Hansen, and Georg Pirrung (DTU). Discussions of early results and conceptualizations with supervisors Andreas Reuter, Claudio Balzani (Leibniz University Hannover), and Holger Hennings (DLR) provided guidance for this work. Guidance and discussions with further colleagues at DLR helped with the setup of the CFD analysis (Christoph Kaiser, Markus Ritter, Diliana Friedewald), and with the analysis of the results (Christoph Kaiser, Christopher Koch, Markus Ritter, David Quero). The authors like to thank all these colleagues for their support.

AI tools (Qwen3 and GPT-OSS) were used to improve the overall readability of the paper. (Re-)formulation suggestions were generated based on original ideas and draft text, which were critically assessed and selectively incorporated.

https://doi.org/10.5194/wes-2026-9
Preprint. Discussion started: 10 February 2026

References

Bangga, G.: Sensitivity of Dynamic Stall Models to Dynamic Excitation on Large Flexible Wind Turbine Blades in Edgewise Vibrations, Energies, 18, 470, https://doi.org/10.3390/en18030470, 2025.

Bisplinghoff, R. L. and Ashley, H.: Principles of Aeroelasticity, John Wiley & Sons Ltd, 1962.

Bottasso, C. L., Campagnolo, F., Croce, A., and Tibaldi, C.: Optimization–based study of bend–twist coupled rotor blades for passive and integrated passive/active load alleviation, Wind Energy, 16, 1149–1166, https://doi.org/10.1002/we.1543, 2013.

Branlard, E., Jonkman, J., Porter, J. H., Vijayakumar, G., Jonkman, B., Singh, M., Mayda, E., and Dixon, K.: A generalized wind turbine cross section as a reduced-order model to gain insights in blade aeroelastic challenges, Journal of Physics: Conference Series (Online), 2767, 022 005, https://doi.org/10.1088/1742-6596/2767/2/022005, 2024.

Chaviaropoulos, P. K.: Flap/lead-lag aeroelastic stability of wind turbine blades, Wind Energy, 4, 183–200, https://doi.org/10.1002/we.55, 2001.

Chaviaropoulos, P. K., Soerensen, N. N., Hansen, M. O. L., Nikolaou, I. G., Aggelis, K. A., Johansen, J., Gaunaa, M., Hambraus, T., von Geyr, H. F., Hirsch, C., Shun, K., Voutsinas, S. G., Tzabiras, G., Perivolaris, Y., and Dyrmose, S. Z.: Viscous and Aeroelastic Effects on Wind Turbine Blades. The VISCEL Project. Part II: Aeroelastic Stability Investigations, Wind Energy, 6, 387–403, https://doi.org/10.1002/we.101, 2003.

Chen, P. C.: Damping Perturbation Method for Flutter Solution: The g-Method, AIAA Journal, 38, 1519–1524, https://doi.org/10.2514/2.1171, 2000.

Chetan, M., Yao, S., and Griffith, D. T.: Flutter Behavior of Highly Flexible Two- and Three-bladed Wind Turbine Rotors, Wind Energy Science Discussions, pp. 1–29, https://doi.org/10.5194/wes-2021-132, 2021.

Collier, W., Ors, D., Barlas, T., Zahle, F., Bortolotti, P., Marten, D., Jensen, C. S. L., Branlard, E., Zalkind, D., and Lønbæk, K.: Aeroelastic code comparison using the IEA 22MW reference turbine, Journal of Physics: Conference Series (Online), 2767, 052 042, https://doi.org/10.1088/1742-6596/2767/5/052042, 2024.

Greenberg, J. M.: Airfoil in sinusoidal motion in a pulsating stream, Tech. Rep. NACA-TN-1326, National Advisory Comittee for Aeronautics, https://ntrs.nasa.gov/citations/19930082116, 1947.

Griffith, D. T. and Chetan, M.: Assessment of flutter prediction and trends in the design of large-scale wind turbine rotor blades, Journal of Physics: Conference Series (Online), 1037, 042 008, https://doi.org/10.1088/1742-6596/1037/4/042008, 2018.

Hansen, M. H.: Aeroelastic stability analysis of wind turbines using an eigenvalue approach, Wind Energy, 7, 133–143, https://doi.org/10.1002/we.116, 2004.

Hansen, M. H.: Aeroelastic instability problems for wind turbines, Wind Energy, 10, 551–577, https://doi.org/10.1002/we.242, 2007.

Hermes, A.: High fidelity aeroelastic stability analysis of complex blades in 3D flow, Phd thesis, DTU Wind and Energy Systems, https://doi.org/10.11581/36dc091b-43b7-4612-a636-f24d22518ef9, 2024.

Hermes, A., Zahle, F., Riva, R., Madsen, J., Bergami, L., and Skovby, C.: High fidelity aeroelastic stability analysis of operating wind turbines, Renewable Energy, 253, 123 424, https://doi.org/10.1016/j.renene.2025.123424, 2025.

Kaiser, C., Thormann, R., Dimitrov, D., and Nitzsche, J.: Time-Linearized Analysis of Motion-Induced and Gust-Induced Airloads with the DLR TAU Code, in: Deutscher Luft- und Raumfahrtkongress 2015, Deutsche Gesellschaft für Luft- und Raumfahrt - Lilienthal-Oberth e.V. (DGLR), https://elib.dlr.de/101278/, 2015.

https://doi.org/10.5194/wes-2026-9
Preprint. Discussion started: 10 February 2026

Kallesøe, B. S.: Effect of steady deflections on the aeroelastic stability of a turbine blade, Wind Energy, 14, 209–224, https://doi.org/10.1002/we.413, 2011.

Kallesøe, B. S. and Kragh, K. A.: Field Validation of the Stability Limit of a Multi MW Turbine, Journal of Physics: Conference Series (Online), 753, https://doi.org/10.1088/1742-6596/753/4/042005, 2016.

Kelley, C. L. and Paquette, J.: Investigation of flutter for large, highly flexible wind turbine blades, Journal of Physics: Conference Series (Online), 1618, 052 078, https://doi.org/10.1088/1742-6596/1618/5/052078, 2020.

Li, A., Gaunaa, M., Pirrung, G. R., Meyer Forsting, A., and Horcas, S. G.: How should the lift and drag forces be calculated from 2-D airfoil data for dihedral or coned wind turbine blades?, Wind Energy Science Discussions, pp. 1–40, https://doi.org/10.5194/wes-2021-163, 2022.

Li, A., Gaunaa, M., and Pirrung, G. R.: Computationally efficient aerodynamic modelling of swept wind turbine blades using coupled near-wake and vortex cylinder models, Wind Energy Science, 10, 2515–2550, https://doi.org/10.5194/wes-10-2515-2025, 2025.

Lobitz, D. W. and Veers, P. S.: Aeroelastic behavior of twist-coupled HAWT blades, Tech. Rep. SAND–97-2448C; AIAA–98-0029; CONF-980104–, Sandia National Laboratories, https://www.osti.gov/biblio/560809, 1998.

Patel, K. and Lefas, D.: Role of Shocks in Transonic Bending-Torsion Flutter, in: AIAA SciTech Forum, The American Institute of Aeronautics and Astronautics, Inc., https://doi.org/10.2514/6.2025-0818, 2025.

Peng, C.: Linearization and Modal Problems in Multibody System Dynamics for Modern Wind Turbines, Ph.D. thesis, Università degli Studi di Parma. Dipartimento di Ingegneria dei sistemi e delle tecnologie industriali, https://www.repository.unipr.it/handle/1889/6352?mode=full, 2025.

Pirrung, G. R., Grinderslev, C., Sørensen, N. N., and Riva, R.: Vortex-induced vibrations of wind turbines: From single blade to full rotor simulations, Renewable Energy, 226, 120 381, https://doi.org/10.1016/j.renene.2024.120381, 2024.

Rasmussen, F., Petersen, J. T., and Madsen, H. A.: Dynamic Stall and Aerodynamic Damping, Journal of Solar Energy Engineering, 121, 150–155, https://doi.org/10.1115/1.2888426, 1999.

Stäblein, A. R., Hansen, M. H., and Pirrung, G.: Fundamental aeroelastic properties of a bend–twist coupled blade section, Journal of Fluids and Structures, 68, 72–89, https://doi.org/10.1016/j.jfluidstructs.2016.10.010, 2017a.

Stäblein, A. R., Hansen, M. H., and Verelst, D.: Modal Properties and Stability of Bend-Twist Coupled Wind Turbine Blades, Wind Energy Science, 2, 343–360, https://doi.org/10.5194/wes-2016-39, 2017b.

Theodorsen, T.: General Theory of Aerodynamic Instability and the Mechanism of Flutter, Tech. Rep. NACA-TR-496, National Advisory Comittee for Aeronautics, https://ntrs.nasa.gov/citations/19930090935, 1949.

Verdonck, H., Hach, O., Polman, J. D., Schramm, O., Balzani, C., Müller, S., and Rieke, J.: Uncertainty quantification of structural blade parameters for the aeroelastic damping of wind turbines: a code-to-code comparison, Wind Energy Science, 9, 1747–1763, https://doi.org/10.5194/wes-9-1747-2024, 2024.

Volk, D., Kallesøe, B., Johnson, S., Pirrung, G., Riva, R., and Barnaud, F.: Large wind turbine edge instability field validation, in: Journal of Physics: Conference Series, vol. 1618, IOP Publishing, Delft, The Netherlands, https://doi.org/10.1088/1742-6596/1618/5/052014, 2020.

Wanke, G., Bergami, L., and Verelst, D. R.: Differences in damping of edgewise whirl modes operating an upwind turbine in a downwind configuration, Wind Energy Science, 5, 929–944, https://doi.org/10.5194/wes-5-929-2020, 2020.

Xia, H., Cheng, H., Zhang, Q., Li, D., and Lin, Z.: Uncertainty analysis of aeroelastic flutter for a large-scale flexible wind turbine blade, Renewable Energy, 256, 124 629, https://doi.org/10.1016/j.renene.2025.124629, 2026.

Zhou, X., Huang, K., and Li, Z.: Effects of bend-twist coupling on flutter limits of composite wind turbine blades, Composite Structures, 192, 317–326, https://doi.org/10.1016/j.compstruct.2018.02.071, 2018.